Investigation and Characterization of the HERA Dish and Feed using Electromagnetic Simulations

by

Mariet Venter

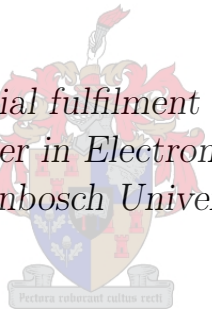

Thesis presented in partial fulfilment of the requirements for the degree of Master in Electronic Engineering at Stellenbosch University

Department of Electrical and Electronic Engineering,
University of Stellenbosch,
Private Bag X1, Matieland 7602, South Africa.

Supervisor: Prof. D.B. Davidson

March 2016

Declaration

By submitting this thesis electronically, I declare that the entirety of the work contained therein is my own, original work, that I am the owner of the copyright thereof (unless to the extent explicitly otherwise stated) and that I have not previously in its entirety or in part submitted it for obtaining any qualification.

Date: March 2016

Abstract

Investigation and Characterization of the HERA Dish and Feed using Electromagnetic Simulations

M. Venter

Department of Electrical and Electronic Engineering,
University of Stellenbosch,
Private Bag X1, Matieland 7602, South Africa.

Thesis: MEng (Electronic)

March 2016

This thesis presents the results of the electromagnetic analysis of the dish and feed for the Hydrogen Epoch of Reionization Array (HERA) experiment. The science goal for HERA is a challenging task in the form of detecting and characterizing the power spectrum of the Epoch of Reionization (EoR).

The HERA faceted parabolic dish is investigated where it is determined that, at the relevant frequencies, the panels forming the dish is not a significant deviation from a perfect paraboloid. However, the screen placed on the dish does cause variations in the gain across frequency. The mutual coupling between several HERA elements is determined not to be significant even without including the screen. Furthermore, at 150 MHz it is found that the HERA dish delivers a Field of View of approximately 9° and sidelobe levels of 15 dB below the main beam, which has a gain of 25 dB. The beam level at the horizon is measured at approximately 40 dB below the main beam. The *uv*-coverage of HERA as an interferometer is calculated for a tight-packed hexagon configuration. With the inclusion of outlier elements, this coverage improves significantly and it is shown that HERA will have excellent imaging capabilities. The delay-spectrum technique used by HERA astronomers is unpacked and applied to the HERA dish using electromagnetic simulations and post-processing. It is determined that reflections off the dish does not meet the −60 dB power after 60 ns specification. Rather, these reflections are measured at −35 dB. Results from modelling and optimization in the frequency domain of alternative feeds for HERA is compared to the current PAPER feed. This includes several versions of the bowtie feed, a scaled PAPER feed and a sinuous feed, which is also manufactured and measured. It is shown that such

an effort in conjunction with a reflector is met with challenges due to the low frequency band.

Uittreksel

Ondersoek en Karakterisering van die HERA Skottel en Voer met behulp van Elektromagnetiese Simulasies

("Investigation and Characterization of the HERA Dish and Feed using Electromagnetic Simulations")

M. Venter

Departement Elektriese en Elektroniese Ingenieurswese,
Universiteit van Stellenbosch,
Privaatsak X1, Matieland 7602, Suid Afrika.

Tesis: MIng (Elektronies)

Maart 2016

Hierdie tesis lewer resultate van die elektromagnetiese ontleding van die *Hydrogen Epoch of Reionization Array* (HERA) eksperiment se skottel en voer. Die uitdagende wetenskapsdoel vir HERA is die opsporing en karakterisering van die Epog van Herionisasie (EoR) se drywing.

Deur 'n ondersoek te doen van die HERA skottel, word dit bepaal dat die panele waaruit die skottel saamgestel is, nie 'n groot afwyking van 'n perfekte parabool veroorsaak nie. Die skerm bo-op die skottel veroorsaak wel variasies in die aanwins teenoor frekwensie. Die wedersydse-koppeling tussen 'n aantal HERA elemente het nie 'n groot invloed nie, selfs sonder die skerm. By 150 MHz word daar gevind dat die HERA skottel 'n sigveld van ongeveer 9° het en sy-lob vlakke van 15 dB minder as die hoofbundel, wat 'n aanwins van 25 dB het. Die drywingspatroon by die horison word gemeet by ongeveer 40 dB minder as die hoofbundel. Die *uv*-dekking van HERA word bereken vir 'n nou-verpakte seshoek konfigurasie. Met die insluiting van wyd-omliggende elemente, verbeter die *uv*-dekking aansienlik en word daar aangedui dat HERA uitstekende beeld-vermoëns sal hê. Die vertraging-spektrum tegniek wat gebruik word deur HERA sterrekundiges word ondersoek en toegepas op die HERA skottel met behulp van elektromagnetiese simulasies en post-verwerking. Dit word vasgestel dat weerkaatsings van die skottel nie voldoen aan die −60 dB seinsterkte na 60 ns spesifikasie nie. Inteendeel, die weerkaatsings word gemeet by −35 dB. Resultate van modellering en optimering in die frekwensiegebied van alternatiewe voere vir HERA word vergelyk

met die huidige PAPER voer. Dit sluit verskeie weergawes van die strikdas-voer, 'n geskaalde PAPER voer en 'n kronkelende voer in, wat ook gebou en getoets is. Daar word aangetoon dat so 'n poging, in samewerking met 'n reflektor, uitdagend is as gevolg van die lae-frekwensie band.

Acknowledgements

Firstly, I would like to express my deepest gratitude to my supervisor, **Prof David B Davidson**, for truly being an example of an excellent engineer as well as a very understanding human being — a combination that is easy to look up to. Thank you for the direction and support that I have continually received from you since I did my final-year project under your supervision. I am also grateful for the numerous opportunities that you have exposed me to — no value can be placed on them.

I also express my gratitude to the entire HERA collaboration for granting me the opportunity to learn from experts in the radio astronomy community. I would specifically like to thank **David deBoer**, **James Aguirre**, **Rich Bradley**, **Eloy de Lera Acedo** and **Aaron Ewall-Wice** for each e-mail, telecon and impartation I have received. To have been involved with HERA has been an unforgettable experience and has definitely fuelled my desire to remain involved in projects that are breaking ground.

I am also grateful for insightful discussions shared with **Dr Dirk de Villiers** — your advice on electromagnetic modelling and especially your intrigue and interest in HERA was a source of inspiration for me.

A big thank you to **Wessel Croukamp**, **Wynand van Eeden** and **Anneke Bester** for hours spent manufacturing and measuring the sinuous antenna. This would not have been possible without your contribution and advice.

To my colleagues in the Penthouse — it has been a privilege to share this period of learning with you. I extend a special word of thanks to **Jacki Gilmore** for always providing technical support and general advice. Also, to **Ngoy Mutonkole**, **Vereese van Tonder**, **David Smith** and **André Young** for allowing me to learn from the 'older crowd' .

I would like to thank **SKA South Africa** for providing funding for the duration of this project as well as opportunities to travel to conferences and meetings, whether it be local or abroad.

I would not have been able to complete this thesis without the unconditional love and support from my parents, **Danie and Louise Venter**. I am forever grateful for granting me the opportunity and resources to pursue being a 'ewige student' in Stellenbosch for a little while longer.

This season was marked by highs and lows, but not one of them was without the presence of my **friends and church family**. I wish to thank those who were always ready to listen and committed to keeping my spirits up.

In conclusion, a degree that at times appeared as a mountain too large to conquer was made as tiny as a molehill by my Lord and Saviour, **Jesus Christ**. This is in His service.

Dedications

This thesis is dedicated to my parents, Danie and Louise Venter.

Contents

List of Figures

List of Tables

Nomenclature

Abbreviations and Acronyms

CEM	Computational Electromagnetics
Co-pol	Co-polarization
EFIE	Electric field integral equation
EM	Electromagnetic
FFT	Fast Fourier Transform
FIT	Finite Integral Technique
FNBW	First Null Beamwidth
FoV	Field of View
FT	Fourier Transform
FWHM	Full-Width at Half Maximum
HBA	High Band Antenna
HERA	Hydrogen Epoch of Reionization
HPBW	Half Power Beamwidth
LBA	Low Band Antenna
LOFAR	Low Frequency Array
MFIE	Magnetic field integral equation
MLFMM	Multilevel Fast Multipole Method
MoM	Method of Moments
MRO	Murchison Radio Observatory
MWA	Murchison Widefield Array
NRAO	National Radio Astronomy Observatory
PAPER	Precision Array for Probing the Epoch of Reionization
PEC	Perfect Electric Conductor
PO	Physical Optics
RMS	Root Mean Square
RWG	Rao-Wilton-Glisson
SKA	Square Kilometre Array
SKA-SA	Square Kilometre Array South Africa

SLL	Sidelobe level
SMA	SubMiniature version A
TBD	To be determined
X-pol	Cross-polarization

Constants

$c =$	2.998×10^8 m/s
$\pi =$	3.141592654

Notations

$\mathcal{A}$	Azimuth
A	Antenna beam pattern
A_{mn}	System matrix
A_{mn}^{near}	Nearfield system matrix
A_{mn}^{far}	Farfield system matrix
A_n	Area of triangle T_n
$\mathbf{b}$	Baseline vector
b_m	Matrix equation source vector
b_x	Baseline in x-direction
b_y	Baseline in y-direction
b_z	Baseline in z-direction
$\mathbf{B}$	Complex magnetic flux density
d	Reflector diameter
D	Baseline length in meters
D_λ	Baseline length in wavelengths
D_{max}	Maximum baseline length in meters
D_{min}	Minimum baseline length in meters
$\mathbf{D}$	Complex electric flux density
e	Error function
$\mathcal{E}$	Elevation
$\mathscr{E}$	Instantaneous electric field strength
$\mathbf{E}$	Complex electric field intensity
$\mathbf{E}_1$	Pattern due to Port 1
$\mathbf{E}_2$	Pattern due to Port 2
$\mathbf{E}^t$	Total electric field
$\mathbf{E}^{inc}$	Incident electric field
$\mathbf{E}^s$	Scattered electric field

$\mathbf{E}_{tan}^{t}$	Tangential total electric field
$\mathbf{E}_{tan}^{inc}$	Tangential incident electric field
$\mathbf{E}_{tan}^{s}$	Tangential scattered electric field
$\mathbf{E}_{dm}$	Differential mode pattern
$\mathbf{E}_{cm}$	Common mode pattern
f	Focal length
f	Frequency
f_{max}	Maximum frequency
$\mathbf{f}_m$	Rao-Wilton-Glisson testing function
$\mathbf{f}_n$	Rao-Wilton-Glisson basis function
F	Filtering function
F	Fringe function
G	Gain of dish with surface errors
G_0	Green's function
G_e	Complex electronics gain
G_f	Feed gain
G_m	Feed gain amplitude
G_{par}	Gain of perfect paraboloid
h	Height
H	Hour angle
$\mathbf{H}$	Complex magnetic field intensity
$\mathbf{H_{inc}}$	Incident magnetic field
$\mathbf{H}^t$	Total magnetic field
$\mathbf{H}^s$	Scattered magnetic field
i	Antenna element index
I	Intensity distribution
j	Antenna element index
$\mathbf{J}_c$	Complex conductive electric current density
$\mathbf{J}_i$	Complex impressed electric current density
$\mathbf{J}_s$	Induced surface current
k	Phase constant
k_0	Free space constant
$\mathscr{K}$	Integral operator
l	Direction cosine on sky
l_n	Length of the nth edge
$\mathcal{L}$	Latitude

$\mathscr{L}$	Integral operator
m	Direction cosine on sky
m_s	Mode number for sinuous antenna
$\mathbf{M}_i$	Complex impressed magnetic current density
n	Direction cosine on sky
n	Gain pattern number
$\hat{n}$	Surface unit vector
N	Number of unknowns
N_{ant}	Number of antennas
N_{bases}	Number of baselines
N_s	Number of sinuous arms
p	Number of radiating cells
r	Radius, spherical coordinates
$\mathbf{r}$	Observation point
$\mathbf{r'}$	Source point
R	Antenna response function
R_H	Inner diameter radius
R_L	Outer diameter radius
R_m	Average input resistance
$\mathbf{s}$	Source direction
S	Source flux
S_o	Object surface
t	Time
$\tan\delta$	Dielectric Loss Tangent
T_n	Triangle n
u	East baseline length in wavelengths
V	Visibility function
V_o	Object volume
V_S	Source volume
V_∞	Exterior region volume
w	Baseline length in wavelengths towards source
X	x-coordinate in wavelengths
Y	y-coordinate in wavelengths
Z	z-coordinate in wavelengths
z_0	Distance from rim of reflector to feed
Z_0	Intrinsic impedance

α	Attenuation constant
α_n	Unknown coefficient
α_p	Angular width
ϵ	RMS surface errors
ϵ_a	Aperture efficiency
δ	Declination
δ_i	Impulse charge
δ_D	Dirac Delta function
δ_p	Rotation angle
$\delta\Delta$	Interferometer resolution
Δ_{max}	Maximum resolution
Δ_{FoV}	Maximum angular resolution
γ	Propagation constant
λ	Wavelength
μ	Permeability
ν	Spatial frequency
ϕ	Azimuth angle, spherical coordinates
ρ_m	Magnetic charge density
ρ_n	Position vector
ρ_v	Electric charge density
σ	Conductivity
τ	Time delay
τ_e	Electric time delay
τ_g	Geometric time delay
τ_p	Growth rate
θ	Polar angle, spherical coordinates
θ_o	Taper Angle
ω	Angular frequency
υ	North baseline length in wavelengths
υ_{out}	Feed output signal
υ_{in}	Feed input signal
ε	Permittivity
ε_r	Relative Permittivity
∇	Differential operator
∇'	Differentiation in source coordinates
*	Conjugate
$\sim$	Fourier transformation

Chapter 1

Introduction

1.1 Background

Radio astronomy began as a side effect to a purely military experiment done in the early 20th century. In 1931, Karl Jansky, who today is recognized as the father of radio astronomy, had the assignment to study the arrival direction of thunderstorm static at a telecommunications lab of Bell Telephone Laboratories [1]. The design was a 30 m long and 3 m high vertically polarized unidirectional antenna that rotated every 20 minutes. Looking at the results, Jansky found a peak at every rotation or when the antenna was directed towards the center of the Milky Way. After Jansky passed away, another astronomer Grote Reber, built the first prototype of the modern radio telescope in 1937 – a 9.5 m parabolic reflector [2]. This discovery led to the design and construction of bigger telescopes around the world as it was realized that different wavelengths need different technology and probe different physics. Also, the amount of information captured is related to the size of the surface of the telescope.

Ever since these early stages, radio astronomy has opened a window into the universe that benefits astronomy and science on numerous levels. When considering wavelengths of the electromagnetic spectrum possessing the characteristic of atmospheric opacity, it can be seen that only optical and radio waves are readily observable from Earth. With the introduction of interferometry in radio astronomy, the amount of energy that can be captured and thus the sensitivity of the telescope have increased significantly as has the resolution. This has never been put more into practice than by the Square Kilometre Array (SKA) project, which is an international collaboration to construct largest radio telescope in the world – intended to be approximately 50 times more sensitive and 10 000 times faster (survey speed) than any existing radio telescopes. The title of the project derives from the collecting areas of the antennas where together they add up to one square kilometer [3]. Some of the science goals of the SKA includes the study of the evolution of galax-

ies, formation of the early stars or the Dark Ages and the study of general relativity theories. The SKA consists of three instruments covering different frequency bands each containing their own science goals, where one of these is the low frequency arrays with a bandwidth of nominally $50 - 250$ MHz.

While many facets of the SKA project are still in development, actual science is already being accomplished by low frequency pathfinders such as the Low Frequency Array (LOFAR) and the Murchinson Widefield Array (MWA). However, the SKA is not the only organization investing in low frequency radio astronomy and the focus throughout this thesis will rest on one such project.

1.2 HERA and the Epoch of Reionization

The Hydrogen Epoch of Reionization Array (HERA) is a collaborative experimental effort between universities and science institutions from the United States, the United Kingdom and South Africa. The project is spearheaded by the University of California, Berkeley with heavy input from the American National Radio Astronomy Observatory (NRAO) and a growing collaboration with SKA South Africa (SKA-SA). The project is divided into three phases - HERA I is already in progress and consists of the merging of the Precision Array for Probing the Epoch of Re-ionization (PAPER) and the MWA. Currently the focus is on HERA II where a grid of 14 m reflector dishes arranged in a close-packed array is under construction on the SKA-SA Karoo site. A picture of the proposed dish with PAPER dipoles as feed is shown in Figure 1.1. HERA III will be implemented in the subsequent decade and will aim to join SKA low frequency science goals.

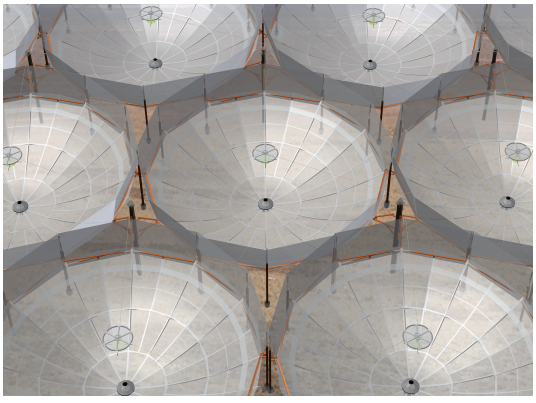

Figure 1.1: A graphical representation of 14m HERA dishes in the Karoo (Source: David deBoer).

However, HERA is first and foremost a focussed experiment with the single science goal the detection and characterization of the power spectrum of the Epoch of Reionization (EoR). This epoch depends on the known presence

of hydrogen in outer space. Before the Dark Ages, ionized hydrogen was widely and smoothly distributed throughout the Universe. Eventually the universe cooled down sufficiently for hydrogen to become neutral and no longer ionized as it had no net electric charge. It is known that neutral gasses have the characteristic of being transparent [4], explaining why it is impossible for astronomers to observe the Dark Ages optically. Over time gravity created more dense hydrogen regions and as the first stars and galaxies began forming it is expected that these hydrogen regions lie between galaxies and in filaments. These dense regions caused the reionization of the hydrogen. Hence, the period during which the hydrogen transitioned from neutral to ionized is known as the EoR.

Once hydrogen is in the neutral state a radio transmission occurs due to the quantum-mechanical spin of the electron [5]. When the electron alternates its spinning direction energy is emitted at a wavelength of 21 cm which correlates to approximately 1420 MHz. However, because of a phenomenon called redshift, astronomers on Earth presently must observe radio waves below 200 MHz to detect the EoR. Redshift can be defined as a shift in the frequency of a photon toward a lower energy or a longer wavelength as it travels through the cosmos away from the observer in an expanding universe [6]. Studying these waves could provide a map of the events as the first stars and galaxies were forming as the interaction of hydrogen with other celestial sources is believed to predict the events of the early Universe. What astronomers hope to see is hydrogen changing from being relatively cold to interacting with the first stars and galaxies to eventually being ionized by all the heat and radiation being emitted in the EoR. However, there are several reasons why the EoR has never been detected by radio astronomers. One of these is the bright signals between Earth and the weak hydrogen emissions, called foreground emission, making it difficult to obtain enough sensitivity to detect the EoR. Also, FM and AM radio transmit below 200 MHz, forcing radio astronomers to search for extremely radio quiet areas to do their EoR observations.

In summary, HERA will address three sets of key questions, namely what were the properties of high redshift galaxies, how did they affect the Universe around them, and does the current cosmological model accurately describe the Universe during the Dark Ages? HERA is intended to be capable of strong characterization and aims to provide the first images of large-scale hydrogen structure.

1.3 Thesis Overview

This thesis contains some of the first work on extensive electromagnetic modelling for the HERA radio telescope experiment. Chapter 2 presents theoretical background applicable to the work in the rest of the thesis including applicable antennas and low frequency arrays. Also, a section on radio interferometry is

presented which includes the definition of the Fourier Transform and the interferometer. The chapter is concluded with an introduction to a filtering method used by radio astronomers called the delay-spectrum technique. The work presented in this thesis is a result of computational electromagnetic (CEM) solving methods. Applicable methods are presented and derived in Chapter 3. Using these methods, in Chapter 4, HERA could be analysed and characterized as a single element and as an interferometer. This chapter also includes an analysis of the HERA dish in terms of allowed reflections against the dish. It is shown that these reflections have a large impact on the instrument's ability to detect the EoR signal. The design and implementation of low frequency feeds are presented in Chapter 5. This thesis concludes in Chapter 6 with a section on contributions made and recommendations for future work.

Chapter 2

Theoretical Background

2.1 Introduction

Before beginning the process of analysing the performance of an antenna or interferometer, it is fundamental to understand both the antenna itself and the analysing methods used for the data obtained by the instrument. This chapter therefore presents some of the theory underlying the above mentioned, specifically with respect to the HERA experiment. Firstly, an overview of relevant antenna types is presented. The next section focuses on the background and working of an interferometer. This chapter concludes with a section on the delay-spectrum technique, a method used to detect the EoR amid bright foregrounds.

2.2 Applicable Antennas

2.2.1 Parabolic Reflector Antenna

Geometrical optics shows that if a ray is directed towards a reflector with parabola as geometrical shape, it will reflect and converge at a spot known as the focal point. This shape is hence understandably used widely in antenna design as a reflector of incident radio waves. Figure 2.1 defines fundamental parameters of a reflector antenna where f is the focal length or distance from the reflector to the feed and d is the diameter of the reflector. Also, z_0 is the distance from the rim of the reflector to the feed. In addition, two other parameters are defined, namely

$$\text{taper angle} = \theta_o = \tan^{-1} \frac{\frac{d}{2}}{z_0} , \tag{2.2.1}$$

$$\text{focal length to diameter ratio} = \frac{f}{d} . \tag{2.2.2}$$

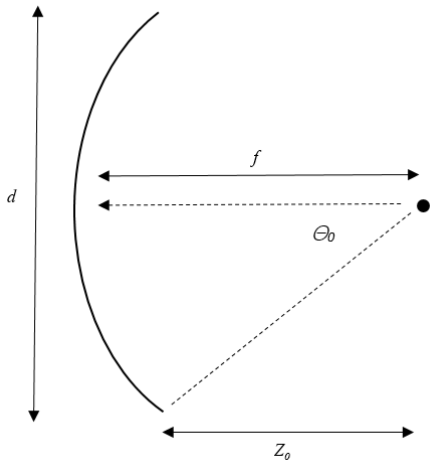

Figure 2.1: A diagram defining applicable parameters of a parabolic reflector.

The taper of a reflector antenna is defined by the pattern of the feed and to what extent it illuminates the rim of the reflector. A -14 dB taper for example, would imply that the pattern from the feed illuminates the edge of the reflector about 14 dB lower than the centre of the reflector. Therefore it is important that a realistic feed be used for the right balance between under-illumination and over-illumination of the reflector's rim. Discussed below are some important figures of merit for parabolic reflectors.

Sidelobe Levels

The lobes of an antenna's radiation pattern can be categorized as main, major, minor, side and back lobes. Increased sidelobe levels (SLL) are undesired because the power is increased in the sidelobes and decreased in the main beam. One method to consider the degree of the increased sidelobes is to measure their level with respect to the maximum value of the main beam.

Aperture Efficiency

The efficiency of a parabolic reflector antenna is dependant on several aspects. One of these is the aperture efficiency ϵ_a which is determined by the gain of the feed G_f and the f/d ratio and defined in [7] as

$$\epsilon_a = \cot^2\left(\frac{\theta_0}{2}\right)\left|\int_0^{\theta_0}\sqrt{G_f(\theta)}\tan\left(\frac{\theta}{2}\right)d\theta\right|^2. \tag{2.2.3}$$

The integration in Equation 2.2.3 can be avoided by approximating the feed pattern as an ideal cosine function as presented by S. Silver in [8]. This function is also circularly symmetric (or not a function of ϕ). Such a gain pattern is written mathematically as

$$G_f(\theta) = \begin{cases} G_m^{(n)} \cos^n(\theta) & 0 \leq \theta \leq \pi/2 \\ 0 & \pi/2 < \theta \leq \pi \end{cases}, \tag{2.2.4}$$

where G_m is the amplitude of the feed gain and can be approximated as $2(n+1)$. Thus, for gain pattern $n = 2$ and a specific f/d ratio the aperture efficiency can be simplified for a certain feed pattern as

$$\epsilon_a = 24 \left\{ \sin^2\left(\frac{\theta_0}{2}\right) + \ln\left[\cos\left(\frac{\theta_0}{2}\right)\right] \right\}^2 \cot^2\left(\frac{\theta_0}{2}\right). \tag{2.2.5}$$

Surface Accuracy

Ruze's equation presented in [9] is used to relate the gain of an antenna or reflector dish to its RMS surface errors. If $G(\epsilon)$ is the gain of a dish with surface errors, where ϵ is the surface RMS errors in meters, then Ruze's equation is defined as

$$G(\epsilon) = G_{par}\, \epsilon^{-\left(\frac{4\pi\epsilon}{\lambda}\right)^2}, \tag{2.2.6}$$

where G_{par} is the gain of a perfect paraboloid without any surface errors.

2.2.2 Sinuous Antenna

The working of the sinuous antenna is derived from principles described in [10] by R.H. DuHamel with the antenna geometry described in his 1987 patent [11]. The sinuous antenna is a frequency-independent antenna where its log-periodic shape is defined by angles and not by lengths. The geometry of the sinuous curve in mathematical form is

$$\phi(r) = (-1)^p\, \alpha_p \sin \frac{\pi \ln \frac{r}{R_H}}{\ln \tau_p}, \tag{2.2.7}$$

where ϕ and r are spherical coordinates at any point along the curve and R_H is the inner antenna radius or feed-point radius which determines the high frequency cut-off. τ_p and α_p represents the cell-to-cell growth rate and angular width, respectively. p indicates the number of radiating cells. An example of a sinuous antenna design is shown in Figure 2.2.

Figure 2.2: A planar sinuous feed with four arms.

The input impedance R_m, of a self-complementary, four-arm planar sinuous antenna in free-space can be obtained by a version of Deschamp's equation. This is defined mathematically in [12] as

$$R_m = \frac{30\pi}{\sin\frac{\pi m_s}{N_s}}\,, \tag{2.2.8}$$

where m_s is the mode number and N_s is the number of arms. The maximum possible modes that can be excited is $(N-1)$. This implies that for a four-arm antenna with one mode the average input resistance seen by a pair of arms is approximately 133 Ohm. The sinuous antenna has a bi-directional radiation pattern with approximately 5.5 dB gain on axis.

2.2.3 Existing Array Elements

As a predecessor to HERA, the PAPER element and feed is fundamental to this thesis and will be presented in detail in later sections. However, to obtain knowledge of antenna elements for low frequency radio astronomy application, investigation and EM analysis of LOFAR and MWA elements are presented in Appendix A.

2.3 Radio Interferometry

By the 1940s it became evident that higher resolution radio telescopes were needed for accurate enough science. However, because of mechanical constraints, building reflector dishes larger than 100 m diameter brings many challenges. This section introduces radio interferometry which produces images of celestial objects by combining observation results. This is done by overlapping the waves captured by several antennas or reflectors working together to form one telescope.

2.3.1 The Fourier Transform in Astronomy

At the foundation of radio astronomy and interferometry is the Fourier transform (FT) which states mathematically that an arbitrarily complex function can be represented as a sum of very simple functions such as sine functions. The well-known definition of this transform and its inverse is, respectively,

$$F(\omega) = \frac{1}{\sqrt{2\pi}} \int_{-\infty}^{+\infty} f(t) e^{-j\omega t} dt \,, \tag{2.3.1}$$

$$f(t) = \frac{1}{\sqrt{2\pi}} \int_{-\infty}^{+\infty} F(\omega) e^{j\omega t} dt \,. \tag{2.3.2}$$

Hence, the FT projects between the time t and the (in this case, angular) frequency ω domain. Convolution is another important operation in astronomy. Among other uses, it is implemented to smooth and filter signals. The convolution of two time signals $g(t)$ and $h(t)$ can be defined as

$$g(t) * h(t) = \int_{-\infty}^{+\infty} g(\tau) h(t - \tau) \, d\tau \,. \tag{2.3.3}$$

An important property of the Fourier transform is the convolution theorem which states that the FT of a convolution is the product of two Fourier transforms. Thus, if $G(\omega)$ and $H(\omega)$ are the transforms of $g(t)$ and $h(t)$, respectively, then the convolution theorem is defined as

$$\mathcal{F}[g(t) * h(t)] = G(\omega) H(\omega) \,. \tag{2.3.4}$$

In the same way the correlation of two signals is defined as

$$g(t) \star h(t) = \int_{-\infty}^{+\infty} g(\tau) h(t + \tau) \, d\tau \,. \tag{2.3.5}$$

When h is an even function the correlation becomes equal to the convolution of the two signals. Another property of the Fourier transform is the cross-correlation theorem which states that the FT of a convolution is the product of two Fourier transforms where one is conjugated. This theorem is defined as

$$\mathcal{F}[g(t) \star h(t)] = G^*(\omega) H(\omega) \,. \tag{2.3.6}$$

Also, when $g = h$ the auto-correlation or the Wiener-Khinchin theorem can be defined as

$$\mathcal{F}[h(t) \star h(t)] = |H(\omega)|^2 \,, \tag{2.3.7}$$

which shows that the FT of the auto-correlation of a signal $h(t)$ delivers the power spectrum $|H(\omega)|^2$ of that signal.

2.3.2 The Working of an Interferometer

An analogy for the working of an interferometer can be found in Thomas Young's early 19th century two-slit experiment which he designed to understand the wave-like properties of light. The experiment set-up included two screens and two little slits as shown in Figure 2.3. The response of these slits are wave patterns that either interfere constructively to form a bright point or interfere destructively to form a dark point.

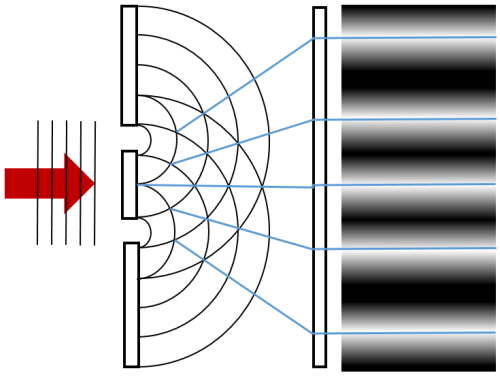

Figure 2.3: A graphical demonstration of Young's two-slit experiment where constructive interference cause cause light and dark patches on 1 optical screen (right).

When Young's experiment is compared to an interferometer it is understood that waves are not radiated, but rather that the antennas are measuring an electromagnetic signal from the sky. Considering two antennas pointed straight up at the zenith and measuring the same light waves from a source not directly above, the waves reach one antenna first and after a small delay reach the second antenna. This is illustrated in Figure 2.4, where D is the baseline length, τ_g is the geometrical delay and τ_e is the electrical delay to counter the geometrical delay. The total delay would equal

$$\tau = \tau_g - \tau_e \,. \tag{2.3.8}$$

Next, the signals are amplified, multiplied and integrated. For this analogy τ_e is zero and the voltage signals are sine waves, which means the integration would equal the average of the product of the waves. Also, the results assume an isotropic primary beam.

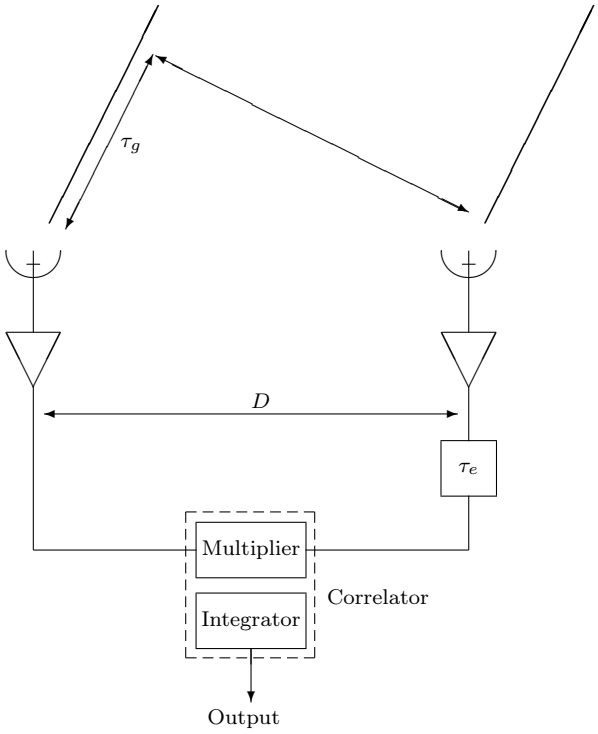

Figure 2.4: A two element interferometer.

In Figure 2.5 the interferometer response of several τ_g instances are shown, assuming that the source under observation can make a 360° rotation around the interferometer. The red and green wave represent the right and left antenna, respectively. The blue wave is the multiplication of the waves whereas the black line is the average. Combining the average over a continuous range of τ_g delivers another sine wave as in the bottom right plot in Figure 2.5. This is called a fringe pattern and is what an interferometer sees across the sky. The distance between the fringes (peaks and troughs) is determined by the length of the baseline whereas the orientation is determined by the orientation of the antennas.

This process is further defined mathematically as shown in [13]. The fringe pattern or function is defined as

$$F = \frac{E^2}{2}[\cos(2\pi\nu\tau_g) + \cos(4\pi t - 2\pi\tau_g)]\,, \tag{2.3.9}$$

where E is the equal magnitude of the signals, ν is the spatial frequency and τ_g is

$$\tau_g = \frac{\mathbf{b}\cdot\mathbf{s}}{c}\,, \tag{2.3.10}$$

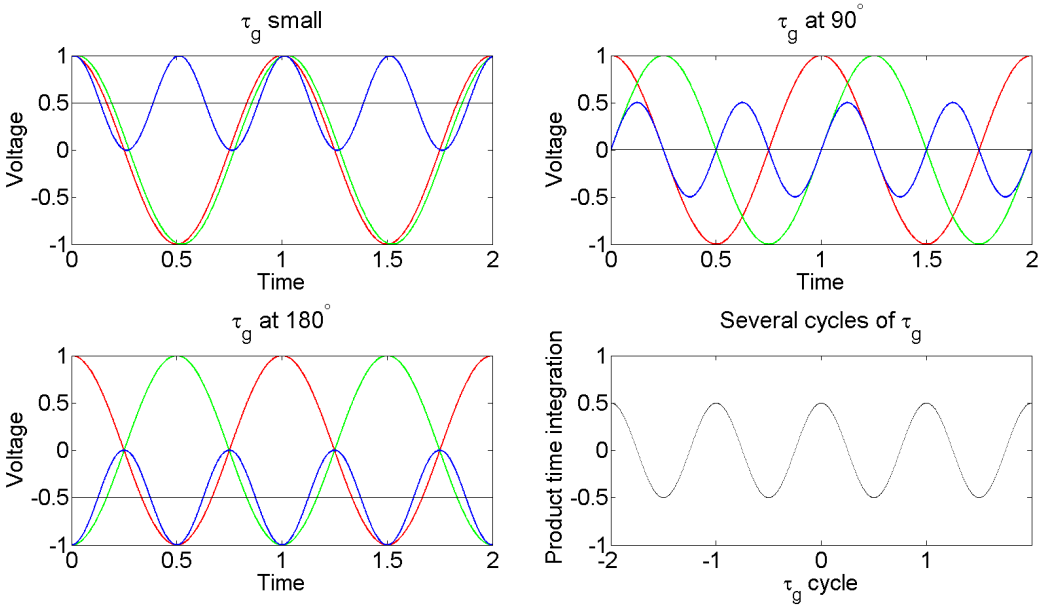

Figure 2.5: Several instances of τ_g for a two-element interferometer showing the voltage signals (red and green), the product of the signals (blue) and the average after correlation (black).

where $\mathbf{b} = (b_x, b_y, b_z)$ is the baseline vector, $\mathbf{s}$ is the source direction and $c = 3 \times 10^{-8}$ is the speed of light in a vacuum. Also

$$\nu\tau_g = \frac{\mathbf{b} \cdot \mathbf{s}}{\lambda} = ul \,, \tag{2.3.11}$$

where $l = \sin\theta$ is the direction cosine for this one dimensional example and u the baseline length in wavelengths. As illustrated in Figure 2.6, the direction cosine alternates between zero at the zenith where $\theta = 0°$ and one at the horizon where $\theta = 90°$.

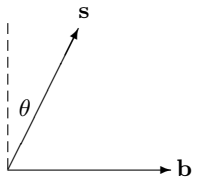

Figure 2.6: The baseline-source relationship.

If the second and more rapid varying term in Equation 2.3.9 is filtered out and Equation 2.3.11 is applied, the fringe function reduces to

$$F = \frac{E^2}{2}\cos(2\pi\nu\tau_g) = \frac{E^2}{2}\cos(2\pi ul)\ . \tag{2.3.12}$$

To recover the intensity distribution or sky brightness I from the interferometer response, the following Fourier transform defines the Interferometric Equation as

$$V(u) = \int I(l)e^{-2\pi i(\mathbf{u}\cdot\mathbf{l})}dl\ , \tag{2.3.13}$$

where V is the complex visibility function derived from the fringe function of the interferometer. A baseline of an interferometer makes one measurement of the visibility function at any one time, which provides an estimate of the sky brightness through a FT.

This concept holds if the interferometer measures the fringe function not on a plane but rather through a volume, which introduces the following appropriate coordinate systems. The antenna baseline vector $\mathbf{b}$ is measured in wavelengths and has length D_λ and components (u, v, w), where u is measured towards the East, v towards the North and w in the direction of the source $\mathbf{s}$. The intensity distribution I has direction cosines (l, m, n) which are measured with respect to (u, v, w) upon Fourier transformation. Thus, the mathematical derivation of the Interferometric equation for non-coplanar interferometers as defined in [13] is

$$V(u,v,w) = \int\int \frac{A(l,m)I(l,m)}{n}\, e^{-2\pi i(ul+vm+wn)}\, dldm\ , \tag{2.3.14}$$

where A describes the antenna beam pattern and $n = \sqrt{1-l^2-m^2}$. In practice, if it can be assumed that all the antennas are positioned on a 2-D plane or that w is small, Equation 2.3.14 reduces to

$$V(u,v) = \int\int A(l,m)I(l,m)\, e^{-2\pi i(ul+vm)}\, dldm\ . \tag{2.3.15}$$

To obtain a good image of a source or a good measurement of the visible sky, good coverage of the uv-plane is needed. The following matrix defines each baseline position by adopting a new earth-based coordinate system (X, Y, Z) specified in wavelengths,

$$\begin{bmatrix} X \\ Y \\ Z \end{bmatrix} = D_\lambda \begin{bmatrix} \cos\mathcal{L}\sin\mathcal{E} - \sin\mathcal{L}\cos\mathcal{E}\cos\mathcal{A} \\ \cos\mathcal{E}\sin\mathcal{A} \\ \sin\mathcal{L}\sin\mathcal{E} + \cos\mathcal{L}\cos\mathcal{E}\cos\mathcal{A} \end{bmatrix}\ , \tag{2.3.16}$$

where $\mathcal{L}$ is the latitude of the observer or interferometer and $(\mathcal{E}, \mathcal{A})$ is the elevation and azimuth of the interferometer. When these components of a new baseline are obtained, the (u, v, w) matrix is given by

$$\begin{bmatrix} u \\ v \\ w \end{bmatrix} = \begin{bmatrix} \sin H & \cos H & 0 \\ -\sin\delta\cos H & \sin\delta\sin H & \cos\delta \\ \cos\delta\cos H & -\cos\delta\sin H & \sin\delta \end{bmatrix} \begin{bmatrix} X \\ Y \\ Z \end{bmatrix} , \tag{2.3.17}$$

where (H, δ) is the hour angle and the declination. The overall angular response of the interferometer is called the synthesized beam which is dependent on how well the uv-plane is sampled. Because of geographical configuration constraints, the uv-plane will never be completely sampled. However, it can be filled in by adding more antennas (i.e. baselines), integrating through time (possible because of the rotation of the Earth) and increasing the bandwidth as the uv-plane is measured in wavelengths. Combining measurements from different antenna configurations will provide different data on different scales of resolution. Short baselines provide data on large scales and long baselines provide data on small scales and together they provide the whole picture. One of the disadvantages of using interferometers is that there is no zero-spacing information, because it is impossible to place elements on top of each other. If there is emission on the sky that is very diffuse, astronomers will never be able to measure it with an interferometer. The following subsection introduces some important properties of interferometers.

2.3.3 Interferometer Properties

This subsection introduces some applicable interferometer properties as defined in [14]. The resolution of a two-element interferometer is proportional to the baseline length. This allows for high resolution without a giant single-dish telescope. The resolution of an interferometer is almost identical to the resolution of a single-dish telescope (difference of factor 1.22) and can be defined as the wavelength λ divided by the maximum baseline length, D_{max},

$$\delta\theta \sim \frac{\lambda}{D_{max}} . \tag{2.3.18}$$

The largest structure that an interferometer is sensitive to is the wavelength divided by D_{min}, the minimum baseline length,

$$\theta_{max} \sim \frac{\lambda}{D_{min}} . \tag{2.3.19}$$

The maximum angular region that the interferometer can see on the sky for a

particular pointing is called the field of view (FoV). It is given as the wavelength divided by d, the diameter of a single dish,

$$\theta_{FoV} \sim \frac{\lambda}{d}\,, \tag{2.3.20}$$

and derives from the Half Power Beamwidth (HPBW) of the primary beam. The total number of baselines N_{bases} with a known number of antennas N_{ant} is defined as

$$N_{bases} = \frac{N_{ant}(N_{ant}-1)}{2}\,. \tag{2.3.21}$$

2.4 The Delay-Spectrum Technique

This section introduces a technique applicable to the processing of data captured by low frequency interferometers looking for large but weak structures such as the EoR. The delay-spectrum technique is first presented in [15] where it is applied to PAPER data. It is important for low frequency arrays where the FoV is large, compared to high frequency arrays where the main beam could be less than a degree, to have the ability to isolate desired sources from brighter foregrounds. A large FoV causes bright sources in the sidelobes of an interferometer to possibly conceal weak sources in the wide primary beam.

The delay-spectrum technique is further applied to 21cm emission data in [16] where the Delay transform (DT) introduced in [15] secures foreground filtering. This technique can be illustrated by using a simple two element, single baseline interferometer as previously shown in Figure 2.4. When tracking a source along the plane parallel to the baseline, it is possible to know where the source is in the sky by knowing its geometrical delay. As mentioned previously, the width of the fringe pattern is a function of the baseline length and also of the bandwidth factor. Taking this into account, the FT of Equation 2.3.15 can be applied to an n number of point sources which delivers

$$V_{ij}(\nu,t) = G_{e,ij}(\nu,t)\sum_{n} A_{ij}(\nu,\mathbf{s}_n(t))S_n(\nu)\; e^{2\pi\nu i(\tau_{g,ijn}(\nu,t)+\tau_{e,ij})}\,, \tag{2.4.1}$$

where i and j are antenna indices, G_e is the complex electronics gain, A is the antenna beam gain as a function of frequency and angle (the product of the voltage patterns for antennas i and j), $\mathbf{s}$ the source direction and S the source flux. The projection of the baseline in the direction of the source is

$$\mathbf{b}\cdot\mathbf{s} = (\cos\delta\cos H)b_x - (\cos\delta\sin H)b_y + (\sin\delta)b_z\,. \tag{2.4.2}$$

Taking Equation 2.3.10 and solving for τ_g results in

$$\tau_g(\nu,t) \equiv \frac{b_x}{c}\cos\delta\cos H - \frac{b_y}{c}\cos\delta\sin H + \frac{b_z}{c}\sin\delta\,, \tag{2.4.3}$$

where $H = h - \alpha$ is a function of sidereal time h of the observer and right ascension α of the source. Because τ_g is frequency-independent, the spectrum $V(\nu,t)$ looks like a fixed delay times frequency due to the exponent multiplication in Equation 2.4.1. Assuming a signal with a spectrum of constant amplitude, the output of the interferometer as a function of the time delay is the FT of the power spectrum of the signal. Hence, all the power will be at a single point and the delay can then be extracted using a FT to transfer between frequency domain and delay domain coordinates. This defines the delay transform (DT) as

$$\begin{aligned}\tilde{V}_{ij}(\tau,t) &= \int_{-\infty}^{\infty} V_{ij}(\nu,t)e^{-2\pi i\nu\tau}d\nu \\ &= \tilde{G}_{e,ij}(\tau,t) * \sum_n \left[\tilde{A}_{ij}(\tau,\mathbf{s}_n(t)) * \tilde{S}_n(\tau) * \delta_D(\tau_{g,ijn} + \tau_{e,ij} - \tau)\right],\end{aligned} \tag{2.4.4}$$

where $\tilde{}$ denotes Fourier transformation. The DT maps intensity from a specific source to a dirac delta function δ_D, centered at the corresponding delay, convolved by frequency-dependent antenna gains and the spectrum of each source.

Emission from a flat-spectrum source cannot be detected by an interferometer baseline if the delay is longer than the baseline as the power will only be visible beyond the maximum delay. By having this knowledge, astronomers can isolate the desired signal from those foregrounds in the delay space. Hence, if the source has a smooth spectrum, a fairly narrow range of values will be centered around a delay position of each instance that a delay is measured. This is the case for foregrounds. However, if the source is not smooth and consists of random lines as is the case for hydrogen, the delay transform will deliver power that is dispersed across the spectrum well beyond the horizon or maximum delay. In this way it is possible to separate the desired signal which lives at higher delays from the undesired signal which lives at low delays. This is demonstrated in Figure 2.7 from [16] where two different baseline lengths are shown.

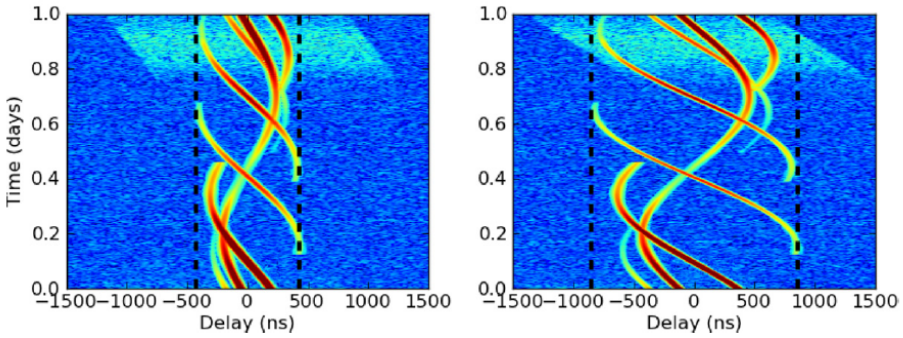

Figure 2.7: A comparison of flat versus unsmooth sources for two different baselines lengths. The maximum baseline or horizon is indicated by black dashed lines. The emission from flat sources remains confined within the horizon limits, while the source with an unsmooth spectrum (cyan at the top) extends beyond these limits.

2.5 Conclusion

This chapter investigated fundamental theory and parameters that form the basis of the aims of this work. It is clear that to successfully observe and analyse data from the early universe, specific antenna and interferometer design is needed. The next chapter introduces electromagnetic software and solution material to aide in the analysing process.

Chapter 3

CEM Solving Methods

3.1 Introduction

This chapter presents selected full-wave CEM solving methods used to analyse antennas electromagnetically. Before unpacking these methods, wave equations as solutions to Maxwell's equations are derived. Maxwell's equations are physical laws which describe how electric and magnetic charges, currents and fields relate to each other and the surroundings they interact with. Solving methods that are unpacked mathematically in this chapter, as described in [17], include the Method of Moments (MoM) and the Multilevel Fast Multipole Method (MLFMM). A short section on time-domain analysis is also included.

3.2 Wave Equations

The instantaneous differential forms of Maxwell's equations are used to solve boundary-value EM problems at any point in space where the field vectors display continuous derivatives. However, in many practical EM problems the time-variations of the source is assumed to be of cosinusoidal form or to be time-harmonic [18]. By representing the time-variations t as e^{jwt}, the fields can be represented only as a function of position (x, y, z). For example, the instantaneous electric field strength $\mathscr{E}$, can be related to its complex form $\mathbf{E}$, as

$$\mathscr{E}(x, y, z; t) = \mathrm{Re}\big[\mathbf{E}(x, y, z)e^{jwt}\big] \,. \tag{3.2.1}$$

Applying this to each instantaneous differential form of Maxwell's equations, delivers the following time-harmonic equations as also described in [18]:

$$\nabla \times \mathbf{E} = -j\omega\mathbf{B} - \mathbf{M}_i \,, \tag{3.2.2}$$

$$\nabla \times \mathbf{H} = \mathbf{J}_i + \mathbf{J}_c + j\omega\mathbf{D} \,, \tag{3.2.3}$$

$$\nabla \cdot \mathbf{D} = \rho_v \,, \tag{3.2.4}$$

$$\nabla \cdot \mathbf{B} = \rho_m \,, \tag{3.2.5}$$

$$\nabla \cdot \mathbf{J}_{ic} = -j\omega\rho_v \,, \tag{3.2.6}$$

where $\mathbf{E}$ and $\mathbf{H}$ is the electric and magnetic field intensity, respectively. $\mathbf{D}$ is the electric flux density, $\mathbf{B}$ is the magnetic flux density, $\mathbf{J}_c$ is the conduction electric current density and $\mathbf{M}_i$ and $\mathbf{J}_i$ is the impressed magnetic and electric current density, respectively. Lastly, ρ_v and ρ_m represents the electric and magnetic charge density, respectively. It is possible to obtain solutions to Maxwell's Equations by solving the directly-related differential equations by increasing them to second order equations called wave equations. To do this, assume a homogeneous medium where the permittivity ε and the permeability μ are constant throughout the material and take the curl of both sides of Equation 3.2.2 and Equation 3.2.3 to deliver

$$\begin{aligned} \nabla \times \nabla \times \mathbf{E} &= -\nabla \times \mathbf{M}_i - \mu\nabla \times (j\omega\mathbf{H}) \\ &= -\nabla \times \mathbf{M}_i - j\omega\mu(\nabla \times \mathbf{H}) \,, \end{aligned} \tag{3.2.7}$$

$$\begin{aligned} \nabla \times \nabla \times \mathbf{H} &= \nabla \times \mathbf{J}_i + \sigma\nabla \times \mathbf{E} + \varepsilon\nabla \times (j\omega\mathbf{E}) \\ &= \nabla \times \mathbf{J}_i + \sigma\nabla \times \mathbf{E} + j\omega\varepsilon(\nabla \times \mathbf{E}) \,, \end{aligned} \tag{3.2.8}$$

where σ is the conductivity. Using the vector identity

$$\nabla \times \nabla \times \mathbf{F} = \nabla(\nabla \cdot \mathbf{F}) - \nabla^2\mathbf{F} \,, \tag{3.2.9}$$

and substituting it into the left side of Equation 3.2.7 while substituting Equation 3.2.3 into the right, Equation 3.2.7 can be rewritten as

$$\begin{aligned} \nabla(\nabla \cdot \mathbf{E}) - \nabla^2\mathbf{E} &= -\nabla \times \mathbf{M}_i - j\omega\nu\big[\mathbf{J}_i + \sigma\mathbf{E} + j\omega\varepsilon\mathbf{E}\big] \\ &= -\nabla \times \mathbf{M}_i - j\omega\nu\mathbf{J}_i - j\omega\mu\sigma\mathbf{E} + \omega^2\mu\varepsilon\mathbf{E} \,. \end{aligned} \tag{3.2.10}$$

Finally, substituting Maxwell's Equation 3.2.4 into Equation 3.2.10, the following uncoupled second-order differential equation for $\mathbf{E}$ is delivered

$$\nabla^2\mathbf{E} = \nabla \times \mathbf{M}_i + j\omega\mu\mathbf{J}_i + \frac{1}{\varepsilon}\nabla\rho_v + j\omega\mu\sigma\mathbf{E} - \omega^2\mu\varepsilon\mathbf{E}\,. \tag{3.2.11}$$

This is known as the vector wave equation for $\mathbf{E}$. The same process can be applied to Equation 3.2.8 using Maxwell's Equation 3.2.5 to obtain the vector wave equation for $\mathbf{H}$ as

$$\nabla^2\mathbf{H} = -\nabla \times \mathbf{J}_i + \sigma\mathbf{M}_i + j\omega\varepsilon\mathbf{M}_i + \frac{1}{\mu}\nabla\rho_m + j\omega\mu\sigma\mathbf{H} - \omega^2\mu\varepsilon\mathbf{H}\,. \tag{3.2.12}$$

For source-free regions where $\mathbf{M}_i = \mathbf{J}_i = \rho_v = \rho_m = 0$, Equation 3.2.11 and Equation 3.2.12, respectively, reduce to

$$\nabla^2\mathbf{E} = j\omega\mu\sigma\mathbf{E} - \omega^2\mu\varepsilon\mathbf{E} = \gamma^2\mathbf{E}\,, \tag{3.2.13}$$

$$\nabla^2\mathbf{H} = j\omega\mu\sigma\mathbf{H} - \omega^2\mu\varepsilon\mathbf{H} = \gamma^2\mathbf{H}\,, \tag{3.2.14}$$

where $\gamma^2 = j\omega\mu\sigma - \omega^2\mu\varepsilon$ or $\gamma = \alpha + jk$ with γ the propagation constant, α the attenuation constant and k the phase constant. These wave equations describe the behaviour of electromagnetic fields in a uniform and conducting medium. An EM field can exist if and only if it satisfies all of Maxwell's Equations or the wave equations.

3.3 Method of Moments

The Method of Moments is a full-wave solution of Maxwell's integral equations in the frequency domain and is also derived in [17]. The Green's function approach is used to obtain the integral equations. Taking the case of an arbitrary perfect electric conductor (PEC) in free space and deriving Maxwell's equations to obtain a solution, an integral equation to solve the currents on the surface of the conductor can be formulated using the Green's function. This function uses a unit source impulse as the driving function to obtain a solution to Maxwell's partial differential equations. Figure 3.1 illustrates a three dimensional object in free space where the volume of the object and the exterior region is denoted, respectively, by V_o and V_∞. Also, $\hat{n}$ is the unit vector on the surface S_o.

If this object is excited by an electric current source of density $\mathbf{J}_i$, the electromagnetic fields $(\mathbf{E}, \mathbf{H})$ will be produced. Acknowledging that there are no tangential E-fields on a PEC surface ($\nabla \cdot \mathbf{E} = 0$), the vector identity in Equation 3.2.9 yields

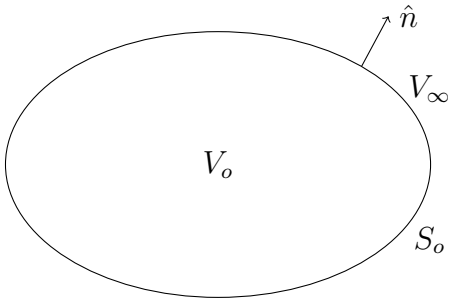

Figure 3.1: An arbitrary three dimensional object in free space.

$$\nabla \times \nabla \times \mathbf{F} = -\nabla^2 \mathbf{F} \,. \tag{3.3.1}$$

Using Equation 3.3.1 and Ohm's law $\mathbf{J} = \sigma \mathbf{E}$, $\mathbf{E}$ and $\mathbf{H}$ both satisfy the vector wave equations of Equation 3.2.13 and Equation 3.2.14

$$\nabla \times \nabla \times \mathbf{E}(\mathbf{r}) - k_0^2 \mathbf{E}(\mathbf{r}) = -jk_0 Z_0 \mathbf{J}_i(\mathbf{r}) \qquad \mathbf{r} \in V_\infty \,, \tag{3.3.2}$$

$$\nabla \times \nabla \times \mathbf{H}(\mathbf{r}) - k_0^2 \mathbf{H}(\mathbf{r}) = \nabla \times \mathbf{J}_i(\mathbf{r}) \qquad \mathbf{r} \in V_\infty \,, \tag{3.3.3}$$

where $\mathbf{r}$ is the observation point and $k_0 = \omega\sqrt{\mu_0 \varepsilon_0}$ is the free space phase constant. The free space intrinsic impedance Z_0 is the square root of μ_0 divided by ε_0. The fields also satisfy the Sommerfeld radiation condition, which mathematically states that there are no reflections in infinite space

$$r\left[\nabla \times \begin{pmatrix} \mathbf{E} \\ \mathbf{H} \end{pmatrix} + jk_0 \hat{r} \times \begin{pmatrix} \mathbf{E} \\ \mathbf{H} \end{pmatrix}\right] = 0 \qquad r \to \infty \,. \tag{3.3.4}$$

The vector wave equations for a lossless medium where $\sigma = 0$ reduce to scalar Helmholtz equations. Assuming the conditions for $\mathbf{E}$ for a lossless and source-free medium, Equation 3.2.13 reduce to

$$\nabla^2 \mathbf{E} = -k_0^2 \mathbf{E} \,. \tag{3.3.5}$$

The next step is to introduce the three-dimensional Green's function G_0 that can be used to derive the integral equations for $(\mathbf{E}, \mathbf{H})$. This function satisfies the scaler Helmholtz equation of Equation 3.3.5

$$\nabla^2 G_0(\mathbf{r}, \mathbf{r}') + k_0^2 G_0(\mathbf{r}, \mathbf{r}') = -\delta_i(\mathbf{r} - \mathbf{r}') \,, \tag{3.3.6}$$

where δ_i denotes the impulse charge and $\mathbf{r}'$ denotes the source point. The Green's function also satisfies the radiation condition of Equation 3.3.4

$$r\left[\frac{\partial G_0(\mathbf{r},\mathbf{r}')}{\partial r} + jk_0 G_0(\mathbf{r},\mathbf{r}')\right] = 0 \qquad r \to \infty\,. \tag{3.3.7}$$

The solution to Equation 3.3.6 and Equation 3.3.7 delivers the definition of the Green's function G_0 as

$$G_0(\mathbf{r},\mathbf{r}') = \frac{e^{-jk_0|\mathbf{r}-\mathbf{r}'|}}{4\pi|\mathbf{r}-\mathbf{r}'|}\,. \tag{3.3.8}$$

Next, by making use of the scalar-vector form of Green's theorem shown in Appendix B and interchanging $V = V_\infty$, $\mathbf{a} = \mathbf{E}$ and $b = G_0$, the following is valid:

$$\begin{aligned}\int_{V_\infty} &[G_0(\nabla\times\nabla\times\mathbf{E}) + \mathbf{E}\nabla^2 G_0 + (\nabla\cdot\mathbf{E})\nabla G_0]\,dV \\ &= \oint_{S_\infty} [(\hat{r}\cdot\mathbf{E})\nabla G_0 + (\hat{r}\times\mathbf{E})\times\nabla G_0 + (\hat{r}\times\nabla\times\mathbf{E})G_0]\,dS \\ &- \oint_{S_o} [(\hat{n}\cdot\mathbf{E})\nabla G_0 + (\hat{n}\times\mathbf{E})\times\nabla G_0 + (\hat{n}\times\nabla\times\mathbf{E})G_0]\,dS\,.\end{aligned} \tag{3.3.9}$$

To expand the left-hand side of Equation 3.3.9, Equation 3.3.2 and Equation 3.3.6 is used to deliver

$$\begin{aligned}\oint_{S_\infty} &\left[-jk_0 Z_0 \mathbf{J}_i G_0 - \mathbf{E}\delta_i(\mathbf{r}-\mathbf{r}') + \frac{jZ_0}{k_0}(\nabla\cdot\mathbf{J}_i)\nabla G_0\right] dV \\ &= -jk_0 Z_0 \int_{V_s}\left[\mathbf{J}_i G_0 - \frac{1}{k_0^2}(\nabla\cdot\mathbf{J}_i)\nabla G_0\right] dV - \begin{cases}\mathbf{E}(\mathbf{r}') & \mathbf{r}'\in V_\infty \\ 0 & \mathbf{r}'\in V_o\end{cases},\end{aligned} \tag{3.3.10}$$

where V_S is the volume of the source where $\mathbf{J}_i \neq 0$. The first integral on the right-hand side of Equation 3.3.9 is zero by using the radiation conditions in Equation 3.3.4 and Equation 3.3.7. This gives Equation 3.3.9 as

$$\begin{aligned}\oint_{S_o} &\left[(\hat{n}\cdot\mathbf{E})\nabla G_0 + (\hat{n}\times\mathbf{E})\times\nabla G_0 + (\hat{n}\times\nabla\times\mathbf{E})G_0\right] dS \\ &- jk_0 Z_0 \int_{V_s}\left[\mathbf{J}_i G_0 - \frac{1}{k_0^2}(\nabla\cdot\mathbf{J}_i)\nabla G_0\right] dV = \begin{cases}\mathbf{E}(\mathbf{r}') & \mathbf{r}'\in V_\infty \\ 0 & \mathbf{r}'\in V_o\end{cases}.\end{aligned} \tag{3.3.11}$$

After switching the primed and unprimed coordinates and assuming conditions without the presence of the object, Equation 3.3.11 becomes

$$\mathbf{E}(\mathbf{r}) = -jk_0 Z_0 \int_{V_s} \left[\mathbf{J}_i G_0 - \frac{1}{k_0^2} (\nabla' \cdot \mathbf{J}_i) \nabla' G_0 \right] dV' \,, \tag{3.3.12}$$

where ∇' denotes differentiation in the source coordinates. Equation 3.3.12 is defined as the incident field which is represented by $\mathbf{E}^{inc}$. Also, using the fact that $\nabla' G_0 = -\nabla G_0$ and letting $\mathbf{a} = \mathbf{H}$, Equation 3.3.11 can also be written, for incident $\mathbf{E}^{inc}$ and $\mathbf{H}^{inc}$, respectively, as

$$\mathbf{E}^{inc}(\mathbf{r}) - \oint_{S_o} \left[(\hat{n}' \cdot \mathbf{E}) \nabla G_0 + (\hat{n}' \times \mathbf{E}) \times \nabla G_0 + jk_0 Z_0 (\hat{n}' \times \mathbf{H}) G_0 \right] dS' = \begin{cases} \mathbf{E}(\mathbf{r}) & \mathbf{r} \in V_\infty \\ 0 & \mathbf{r} \in V_o \end{cases} , \tag{3.3.13}$$

$$\mathbf{H}^{inc}(\mathbf{r}) - \oint_{S_o} \left[(\hat{n}' \cdot \mathbf{H}) \nabla G_0 + (\hat{n}' \times \mathbf{H}) \times \nabla G_0 + jk_0 Y_0 (\hat{n}' \times \mathbf{E}) G_0 \right] dS' = \begin{cases} \mathbf{H}(\mathbf{r}) & \mathbf{r} \in V_\infty \\ 0 & \mathbf{r} \in V_o \end{cases} , \tag{3.3.14}$$

where

$$\mathbf{H}^{inc}(\mathbf{r}) = \int_{V_s} \mathbf{J}_i \times \nabla' G_0 \, dV' \,. \tag{3.3.15}$$

By surface vector analysis it is shown that

$$\hat{n}' \cdot \mathbf{E} = \frac{jZ_0}{k_0} \nabla' \cdot (\hat{n}' \times \mathbf{H}) \,, \tag{3.3.16}$$

$$\hat{n}' \cdot \mathbf{H} = \frac{Y_0}{k_0} \nabla' \cdot (\hat{n}' \times \mathbf{E}) \,. \tag{3.3.17}$$

Finally, applying these equations to Equation 3.3.13 and Equation 3.3.14, they can be written as

$$\mathbf{E}^{inc}(\mathbf{r}) - \oint_{S_o} \left[\frac{jZ_0}{k_0} \nabla' \cdot (\hat{n}' \times \mathbf{E}) \nabla G_0 + (\hat{n}' \times \mathbf{E}) \times \nabla G_0 + jk_0 Z_0 (\hat{n}' \times \mathbf{H}) G_0 \right] dS' = \begin{cases} \mathbf{E}(\mathbf{r}) & \mathbf{r} \in V_\infty \\ 0 & \mathbf{r} \in V_o \end{cases} , \tag{3.3.18}$$

$$\mathbf{H}^{inc}(\mathbf{r}) - \oint_{S_o} \left[\frac{Y_0}{k_0} \nabla' \cdot (\hat{n}' \times \mathbf{H}) \nabla G_0 + (\hat{n}' \times \mathbf{H}) \times \nabla G_0 + jk_0 Y_0 (\hat{n}' \times \mathbf{E}) G_0 \right] dS' = \begin{cases} \mathbf{H}(\mathbf{r}) & \mathbf{r} \in V_\infty \\ 0 & \mathbf{r} \in V_o \end{cases} . \quad (3.3.19)$$

To write these in a more compact form, the definition of integral operators $\mathscr{L}$ and $\mathscr{K}$ is introduced

$$\mathscr{L}(\mathbf{X}) = jk_0 \oint_{S_o} \left[\mathbf{X}(\mathbf{r}) G_0(\mathbf{r}, \mathbf{r}') + \frac{1}{k_0^2} \nabla' \cdot \mathbf{X}(\mathbf{r}') \nabla G_0(\mathbf{r}, \mathbf{r}') \right] dS' , \quad (3.3.20)$$

$$\mathscr{K}(\mathbf{X}) = \oint_{S_o} \mathbf{X}(\mathbf{r}') \times \nabla G_0(\mathbf{r}, \mathbf{r}') \, dS' , \quad (3.3.21)$$

as well as the equivalent surface currents

$$\bar{\mathbf{J}}_s(\mathbf{r}') = \hat{n}' \times \bar{\mathbf{H}}(\mathbf{r}') = Z_0 \hat{n}' \times \mathbf{H}(\mathbf{r}') , \quad (3.3.22)$$

$$\mathbf{M}_s(\mathbf{r}') = \mathbf{E}(\mathbf{r}') \times \hat{n}' , \quad (3.3.23)$$

where $\bar{\mathbf{J}}_s = Z_0 \mathbf{J}_s$ and $\bar{\mathbf{H}} = Z_0 \mathbf{H}$. Finally, Equation 3.3.18 and Equation 3.3.19 can be written as

$$\mathbf{E}^{inc}(\mathbf{r}) - \mathscr{L}(\bar{\mathbf{J}}_s) + \mathscr{K}(\mathbf{M}_s) = \begin{cases} \mathbf{E}(\mathbf{r}) & \mathbf{r} \in V_\infty \\ 0 & \mathbf{r} \in V_o \end{cases} , \quad (3.3.24)$$

$$\bar{\mathbf{H}}^{inc}(\mathbf{r}) - \mathscr{L}(\mathbf{M}_s) - \mathscr{K}(\bar{\mathbf{M}}_s) = \begin{cases} \bar{\mathbf{H}}(\mathbf{r}) & \mathbf{r} \in V_\infty \\ 0 & \mathbf{r} \in V_o \end{cases} , \quad (3.3.25)$$

where $\mathscr{L}$ and $\mathscr{K}$ would denote the scattered fields. To derive integral equations for $\bar{\mathbf{J}}_s$ and $\mathbf{M}_s$ the cross-product of Equation 3.3.24 and Equation 3.3.25 with $\hat{n}$ can be taken while $\mathbf{r}$ approach S_o. Accommodating for the singular point where $\mathbf{r} = \mathbf{r}'$, then

$$\frac{1}{2} \mathbf{M}_s - \hat{n} \times \mathscr{L}(\bar{\mathbf{J}}_s) + \hat{n} \times \tilde{\mathscr{K}}(\mathbf{M}_s) = -\hat{n} \times \mathbf{E}^{inc}(\mathbf{r}) \qquad \mathbf{r} \in S_o , \quad (3.3.26)$$

$$\frac{1}{2} \bar{\mathbf{J}}_s + \hat{n} \times \mathscr{L}(\mathbf{M}_s) + \hat{n} \times \tilde{\mathscr{K}}(\bar{\mathbf{J}}_s) = \hat{n} \times \bar{\mathbf{H}}^{inc}(\mathbf{r}) \qquad \mathbf{r} \in S_o , \quad (3.3.27)$$

which is known as the electric field integral equation (EFIE) and the magnetic field integral equation (MFIE) in vector form for three-dimensional fields, respectively. These integral equations couple the incident electric and magnetic fields to the induced surface current. In simple form, these integral equations represent the superposition of the incident fields and the scattered fields $(\mathbf{E}^s, \mathbf{H}^s)$ to obtain the total field defined mathematically as

$$\mathbf{E}^t = \mathbf{E}^{inc} + \mathbf{E}^s \,, \tag{3.3.28}$$

$$\mathbf{H}^t = \mathbf{H}^{inc} + \mathbf{H}^s \,. \tag{3.3.29}$$

Because the object in Figure 3.1 is an arbitrary PEC which is always lossless, tangential fields cannot exist on the surface and thus $\mathbf{E}^t$ satisfies the boundary condition

$$\hat{n} \times \mathbf{E}^t(\mathbf{r}) = \mathbf{E}^t_{tan}(\mathbf{r}) = 0 \qquad \mathbf{r} \in S_o \,, \tag{3.3.30}$$

and in effect $\mathbf{M}_s = 0$ and $\mathbf{E}^s_{tan} = -\mathbf{E}^{inc}_{tan}$. Thus, Equation 3.3.26 and Equation 3.3.27 reduces to

$$\hat{n} \times \mathscr{L}(\bar{\mathbf{J}}_s) = \hat{n} \times \mathbf{E}^{inc}(\mathbf{r}) \qquad \mathbf{r} \in S_o \,, \tag{3.3.31}$$

$$\frac{1}{2}\,\bar{\mathbf{J}}_s + \hat{n} \times \tilde{\mathscr{K}}(\bar{\mathbf{J}}_s) = \hat{n} \times \bar{\mathbf{H}}^{inc}(\mathbf{r}) \qquad \mathbf{r} \in S_o \,. \tag{3.3.32}$$

The current $\mathbf{J}_s$ can thus also be expressed in an integral equation

$$\mathscr{L}(\bar{\mathbf{J}}_s) = \mathbf{E}^s_{tan} \,, \tag{3.3.33}$$

where the Green's function from Equation 3.3.8 is the driving function for the integral operator $\mathscr{L}$, which maps $\mathbf{J}_s$ to $\mathbf{E}^s_{tan}$. However, it is not generally possible to solve the EFIE analytically. Thus, to obtain the induced surface current $\mathbf{J}_s$, the geometry of the surface is split up into small elements or in this case triangular patches. This process of subdividing the model geometry is called discretization or meshing and is illustrated in Figure 3.2.

$\mathbf{J}_s$ is found by being approximated on each element or patch by an unknown coefficient α and multiplied by a simple function called a basis function. A popular choice described in [19] is the Rao-Wilton-Glisson (RWG) function. This function is defined over two elements sharing a mutual edge. With l_n representing the length of the nth edge, $A_n^{\pm}$ the area of triangle $T_n^{\pm}$ and $\rho_n^{\pm}$ the position vector, the RWG function is defined as

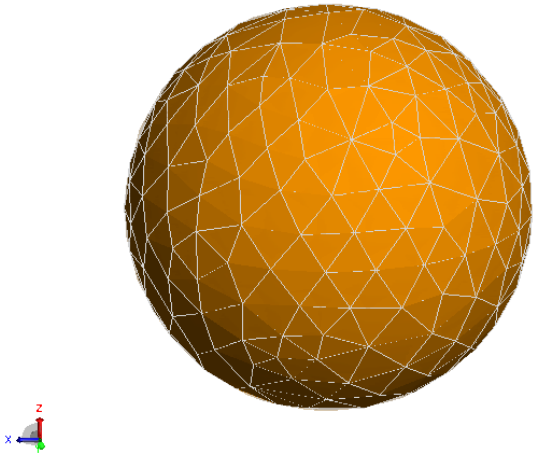

Figure 3.2: A sphere as modelled in FEKO showing the triangular surface mesh used by MoM.

$$\mathbf{f}_n(\mathbf{r}) = \begin{cases} \frac{l_n}{2A_n^+}\rho_n^+ & \mathbf{r} \in T_n^+ \\ \frac{l_n}{2A_n^-}\rho_n^- & \mathbf{r} \in T_n^- \end{cases} . \tag{3.3.34}$$

Thus, the current on each element is

$$\bar{\mathbf{J}}_s = \sum_{n=1}^{N} \alpha_n \cdot \mathbf{f}_n \, , \tag{3.3.35}$$

where N is the number of unknowns or the number of mutual triangle edges. Substituting Equation 3.3.35 into Equation 3.3.33 delivers

$$\sum_{n=1}^{N} \alpha_n \mathscr{L}(\mathbf{f}_n) = \mathbf{E}_{tan}^s \, . \tag{3.3.36}$$

However, α is still unknown. Equation 3.3.36 can be converted into a matrix equation by using a testing or weighting function and integrating over the surface S. In this case the testing function $\mathbf{f}_m (m = 1, 2, ..., N)$ is the same RWG function used as the basis function. This delivers

$$\sum_{n=1}^{N} \alpha_n \int_s \mathbf{f}_m(\mathbf{r}) \int_s G_0(\mathbf{r}, \mathbf{r}') \mathbf{f}_n(\mathbf{r}') \, dS' \, dS$$
$$= \int_s \mathbf{f}_m(\mathbf{r}) \mathbf{E}_{tan}^s \, dS \qquad m = 1, 2, ..., N \, , \tag{3.3.37}$$

which can be written in compact form as a set of linear algebraic equations, where $\langle \bullet \rangle$ denotes integration over the whole surface, as

$$\sum_{n=1}^{N} \alpha_n \langle \mathbf{f}_m, \mathscr{L}(\mathbf{f}_n) \rangle = \langle \mathbf{f}_m, \mathbf{E}^s_{tan} \rangle \qquad m = 1, 2, ..., N \,. \tag{3.3.38}$$

Furthermore, this can also be written as a matrix equation

$$[A]\{\alpha\} = \{b\} \qquad m, n = 1, 2, ..., N \,, \tag{3.3.39}$$

where the system matrix A_{mn} describes the interaction between the nth and the mth element or between the sources represented by basis and testing functions. In mathematical terms A_{mn} is

$$A_{mn} = \langle \mathbf{f}_m, \mathscr{L}(\mathbf{f}_n) \rangle \qquad m, n = 1, 2, ..., N \,, \tag{3.3.40}$$

and $\{\alpha\}$ and $\{b\}$ are the unknown and source vectors, respectively, with $\{b\}$ defined as

$$b_m = \langle \mathbf{f}_m, \mathbf{E}^s_{tan} \rangle \qquad m, n = 1, 2, ..., N \,. \tag{3.3.41}$$

Finally, solving the matrix for α in Equation 3.3.39 can deliver an approximate solution for the surface currents $\mathbf{J}_s$. The MoM has the advantage of not requiring meshing of the free space region as it does not form part of the calculations. This is not the case for methods based on Maxwell's differential equations. Another advantage is that boundary conditions do not have to be set as they are included in the integrals. The memory requirements are determined by the size of the geometry to be analyzed since the discretization determines the size of the matrix [20].

3.4 Multilevel Fast Multipole Method

The Multilevel Fast Multipole Method originates from the same foundation as the MoM, but is applicable to electrically large structures. The basis functions that model the interaction between all triangles are grouped together and computed approximately instead of the full interaction between each basis function (as in the MoM). To do this, matrix A_{mn} of Equation 3.3.39 is split into two parts consisting of nearfield and farfield interactions

$$A_{mn} = A^{near}_{mn} + A^{far}_{mn} \qquad m, n = 1, 2, ..., N \,, \tag{3.4.1}$$

where A^{near}_{mn} is solved using normal MoM described in the previous subsection. However, A^{far}_{mn} is solved using a low-ranked factorized version of the matrix

based on a series expansion of the homogeneous space Green's function. In matrix A_{mn} the diagonal entries represent self-interactions and the remaining entries represent mutual interactions. The latter become weaker as the distance between the basis and testing functions increase. To demonstrate the function of a factorized low-ranked matrix, consider A_{mn}, according to [17], in integral form

$$A_{mn} = \int_s \int_s \mathbf{f}_m(\mathbf{r}) G_0(\mathbf{r}, \mathbf{r}') \mathbf{f}_n(\mathbf{r}') \, dS' \, dS \qquad m, n = 1, 2, ..., N \, . \tag{3.4.2}$$

Next, approximate $G_0(\mathbf{r}, \mathbf{r}')$ by multiple product terms of two functions x and y and add the error function e to obtain the factorized Green's function as

$$G_0(\mathbf{r}, \mathbf{r}') = \sum_{r=1}^{R} x_r(\mathbf{r}) y_r(\mathbf{r}') + e(\mathbf{r}, \mathbf{r}') \, . \tag{3.4.3}$$

This leads to the redefinition of A_{mn} as

$$A_{mn} = \sum_{r=1}^{R} u_{mr} v_{rn} + e_{mn} \tag{3.4.4}$$

where

$$u_{mr} = \int_s \mathbf{f}_m(\mathbf{r}) x_r(\mathbf{r}) \, dS \qquad m = 1, 2, ..., N; r = 1, 2, ..., R \, , \tag{3.4.5}$$

$$v_{rn} = \int_s \mathbf{f}_n(\mathbf{r}') y_r(\mathbf{r}') \, dS' \qquad n = 1, 2, ..., N; r = 1, 2, ..., R \, , \tag{3.4.6}$$

$$e_{mn} = \int_s \int_s \mathbf{f}_m(\mathbf{r}) e(\mathbf{r}, \mathbf{r}') \mathbf{f}_n(\mathbf{r}') \, dS' \, dS \qquad m, n = 1, 2, ..., N \, . \tag{3.4.7}$$

The rank-R matrix $[A]_{N \times N}$ can then be written as

$$[A]_{N \times N} = [u]_{N \times R} [v]_{R \times N} + [e]_{N \times N} \, . \tag{3.4.8}$$

Equation 3.4.8 can be represented by $2RN$ numbers instead of M^2 numbers which is also the case for the number of operations for its multiplication with a vector. This multiplication can be evaluated with fewer operations when R is much smaller than N. Thus, with the MLFMM an acceleration of the matrix-vector product takes place. As can be seen in Table 3.1 from [21] the memory

usage of the MLFMM is much less than the MoM for specific applications. A disadvantage of the MLFMM is that it is not appropriate for modelling of structures containing complex dielectric components.

Application and Frequency	Number of Unknowns	Memory (MoM)	Memory (MLFMM)
• Military aircraft at 690 MHz • Ship (115m x 14m) at 107 MHz • Reflector antenna with aperture size 19 λ	100 000	150 GByte	1 GByte
• Military aircraft at 1.37 GHz • Ship (115m x 14m) at 214 MHz • Reflector antenna with aperture size 38 λ	400 000	2.4 TByte	4.5 GByte
• Military aircraft at 2.65 GHz • Ship (115m x 14m) at 414 MHz • Reflector antenna with aperture size 73 λ	1 500 000	33.5 TByte	18 GByte

Table 3.1: General memory estimates of MoM and MLFMM for different applications.

3.5 Time-domain Analysis

Time-domain analysis is used as a means to investigate properties of an antenna as a function of time. One method in which these results were obtained in this thesis is the time analysis capabilities in POSTFEKO. An EM scattering problem is solved in the frequency domain using MoM or MLFMM with a Fast Fourier Transform (FFT) implemented to obtain the results in the time-domain.

For cases where CST is used, the EM problem is solved directly in the time-domain. The Transient Solver, based on the Finite Integration Technique (FIT) calculates how fields evolve through time at discrete locations. The FIT is a solver based on the integral form of Maxwell's equations and first proposed in [22]. Instead of discretizing or meshing the surface current as for the MoM and MLFMM, the FIT calculates the unknown electric and magnetic fields discretized on a staggered grid.

3.6 Conclusion

This chapter mainly offered a thorough look at specific full-wave EM solving methods used to analyse the work in this thesis. The MoM and MLFMM

played a central role in obtaining information to make accurate conclusions in terms of the performance of HERA and feeds designed for the instrument. The next chapter then investigates the HERA dish, both as a single element and in an array.

Chapter 4

HERA Analysis

4.1 Introduction

Before considering different feeds for HERA, it is important to understand the specifications in terms of the performance of the telescope. This section lays out performance specifications and investigates the 14 meter faceted reflector dish using electromagnetic modelling and analysis. Also, HERA as an interferometer is investigated. Finally, the delay-spectrum technique described in Chapter 2 is applied to HERA.

4.2 Performance Specifications

Listed in Table 4.1 are applicable performance specifications for the HERA experiment. As mentioned in the first chapter of this thesis, EoR emission is expected to be detected below 200 MHz. Hence, the frequency range for HERA is specified as:

$$\begin{aligned} \text{Operating range: } & 108 - 200 \text{ MHz}, \\ \text{Extended range: } & 60 - 200 \text{ MHz}. \end{aligned}$$

It is required that HERA has substantially more collecting area per feed than the current PAPER design. This leads to a design based on a parabolic dish with a feed suspended over the dish. It was determined in [23] that the best efficiency would be delivered at a focal ratio of

$$f/d = 0.32\,.$$

Also, based on the number of acceptable reflections (within certain power limits) between the feed and the dish, the maximum dish diameter is determined as

$$d = 14\text{m}\,,$$

which leads to a focal length of

$$f = 4.5\text{m} .$$

Parameter	**Value**
Frequency range	$108-200$ MHz (performance), $60-200$ MHz (extended)
Diameter	14 m
Focal length	4.5 m ($f/d = 0.32$)
Geometrical optics	prime focus, faceted paraboloid
FoV @ 150 MHz	9°
SLL @ 150 MHz	TBD
Maximum Gain @ 150 MHz	TBD
Beam near horizon @ 150 MHz	< -40 dB compared to zenith
Cross-polarization	TBD
Gain variation across frequency	TBD
Reflections	-60 dB at 60 ns
Surface accuracy	75 mm
Characteristic Impedance	50 Ohm (LNA)

Table 4.1: HERA performance specifications.

The FoV for the HERA dish at 150 MHz is approximately 9° which is significantly narrower than array elements of PAPER, LOFAR and MWA. The cross-polarization, maximum gain and sidelobe level (SLL) at 150 MHz, and gain variation across frequency specifications has not yet (by the time of this thesis submission) been determined by HERA collaborators. A recommendation based on HERA EM results is presented throughout this thesis. The unconventional reflections specification of -60 dB at 60 ns based on the delay-spectrum technique discussed in Chapter 2.4, will be presented in a separate subsection.

The HERA dish is made from wire mesh and since it will be difficult to maintain a perfect paraboloid simply with wire, a faceted paraboloid is designed. The effect of a "sag" on the panels will be investigated in a later subsection. The surface accuracy of a reflector determines the frequencies at which the telescope can operate. A rule of thumb value for the surface accuracy is $\lambda/20$ or 75 mm at a frequency of 200 MHz.

The characteristic impedance for the current HERA system is 50 Ohm. However, for PAPER a matching network is designed to convert from 125 Ohm at the PAPER ports to 50 Ohm for the system. Hence for the remainder of this thesis the PAPER feed is referenced to 125 Ohm and succeeding feeds also thus referenced to obtain the maximum operating band.

4.3 Reflector Dish Analysis

A FEKO model of the faceted dish is shown in Figure 4.1, where a 2 m high screen with a vertical tilt of 8.6° is placed on top of the dish. The cone in the center of the dish is to prevent multiple vertical reflections between the dish and the feed. The feed is (for EM purposes) the only object blocking the dish as the feed and backplane is held aloft by three thin wires extending to higher poles.

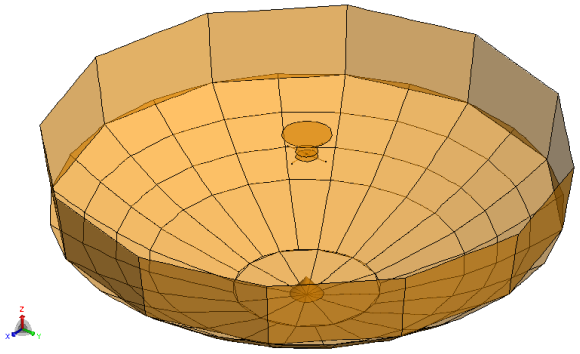

Figure 4.1: FEKO model of the HERA faceted 14 meter reflector dish with PAPER feed and backplane.

MLFMM was used in FEKO to analyse the dish with the current PAPER feed as this is the intended design for the first 127 elements. For 61 linearly spaced points between 50 MHz and 200 MHz, the gain of the dish at zenith is shown in Figure 4.2. Without the screen the gain is moderate to high between 13 dB and 25 dB without rapidly varying across the band, which is desirable. However, with the inclusion of the screen, a dip in the gain at approximately 80 MHz is visible. This is due to waves reflecting off the screen and interfering destructively. Also, increasing the screen's tilt decreases the size of the dip. Further simulations show a decrease in the dip when the backplane is removed. As expected, this trade-off causes less gain across the band. The screen is thought important to reduce mutual coupling between the elements as the HERA elements are closely packed together. Whether this is a legitimate concern and whether the screen achieves this function will be investigated in a following subsection.

It is feasible to use a perfect paraboloid and cylindrical screen as EM representation of the HERA dish, as the difference in results are negligible at these low frequencies and the difference in simulation time small. For the remainder of this thesis a perfect paraboloid is used unless otherwise specified. However, it is taken into consideration that the cylindrical screen causes more gain variation across frequency (no tilt also equals biggest dip).

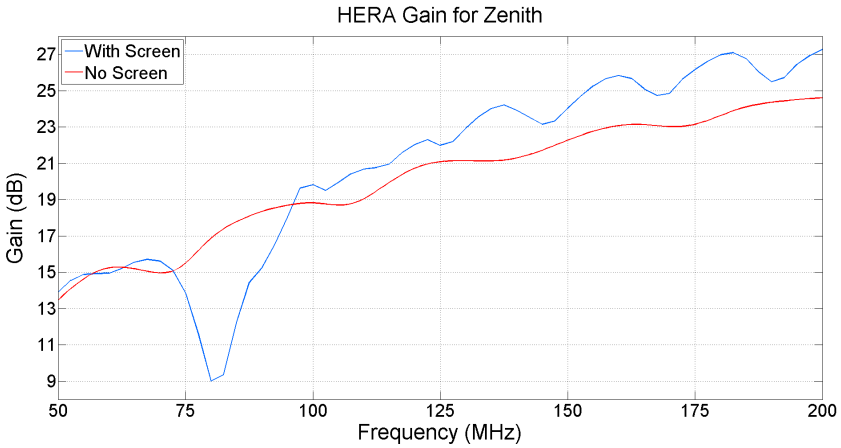

Figure 4.2: The gain of the HERA faceted dish across frequency for $\theta = 0$ and $\phi = 0$.

Figure 4.3 shows the X-pol gain compared to the co-pol gain at 150 MHz for the HERA dish. The sidelobes of the X-pol gain at $\phi = 45°$ is problematic with a value of -21 dB compared to the main beam.

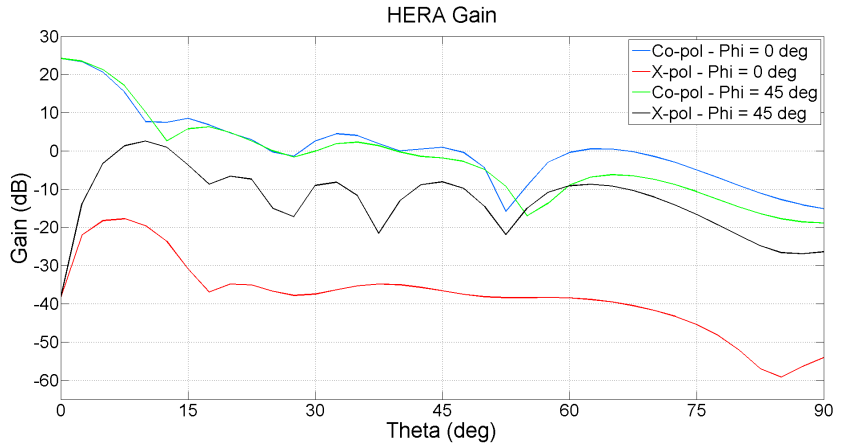

Figure 4.3: Co-pol and X-pol gain at 150 MHz across theta for the HERA dish.

The three dimensional radiation pattern at 150 MHz is shown in Figure 4.4 and the beam patterns for different frequencies at $\phi = 0$ is shown in Figure 4.5. Important performance parameters obtained from these patterns are listed in Table 4.2. If measured against the appropriate specifications at 150 MHz listed in Table 4.1, a few comments can be made. Firstly, the FoV at this frequency is correctly determined as approximately 9° with a maximum gain of 24.01 dB. This is almost a 13 dB improvement compared to the PAPER element. The beam near horizon compared to zenith is less than a decibel under the specified value in Table 4.1 at 150 MHz. Furthermore, a recommendation on the SLL and the maximum gain can be made as 15 dB and 24 dB approximately. This is

not an especially good SLL value for a parabolic reflector, but can be expected at these low frequencies.

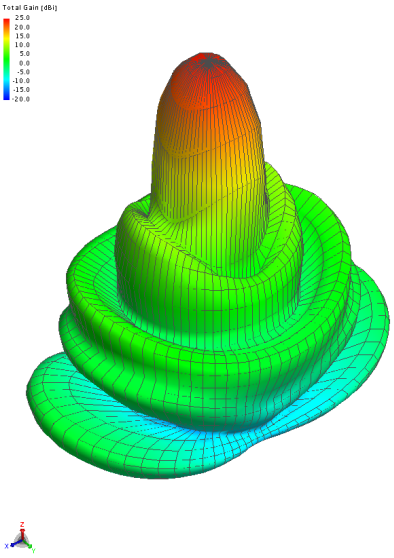

Figure 4.4: The radiation pattern at 150 MHz for the HERA dish.

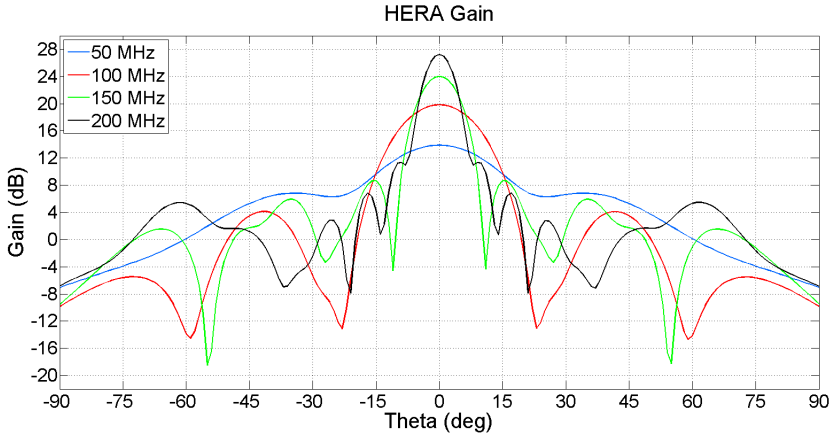

Figure 4.5: The beam pattern of the HERA dish at $\phi = 0$ for various frequencies.

The currents illuminated at 150 MHz on the HERA dish by the PAPER feed is shown in Figure 4.6. The linear colour scale is fixed from zero to 2 mA and shows weak illumination of the dish.

4.3.1 Surface Accuracy & Efficiency

The surface accuracy of the HERA dish is calculated by Ruze's equation defined in Chapter 2. The RMS from two versions of the HERA dish is calculated.

Frequency	FoV	SLL	Beam near Hor.	Max Gain
50 MHz	24.86°	7.04 dB	20.92 dB	13.88 dB
100 MHz	17.37°	15.68 dB	28.7 dB	19.55 dB
150 MHz	9.24°	15.63 dB	39.31 dB	24.01 dB
200 MHz	6.49°	14.11 dB	34.21 dB	27.26 dB

Table 4.2: HERA dish performance based on FEKO simulations.

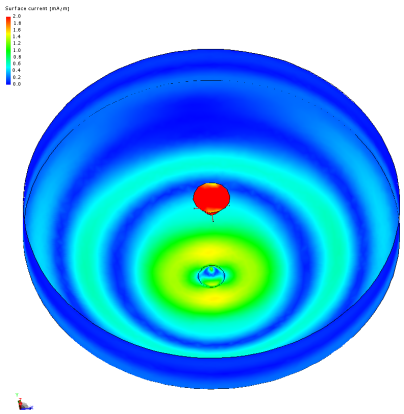

Figure 4.6: Instantaneous currents as illuminated on a HERA dish by the PAPER feed at 150 MHz with a phase of 90°.

One dish is a perfect paraboloid which implies that all incoming waves hitting the dish effectively reach the feed placed at the focal point. The second dish is the HERA faceted dish where the RMS value is calculated to determine the effect of a 'sag' incorporated into a wire mesh panel. It is expected that flat panels (tight wires) would cause deviation of the incoming waves. Figure 4.7 proves this as a RMS value of 87 mm is calculated by Ruze's equation, which is above the rule of thumb value. As mentioned in Chapter 4.2 the acceptable accuracy of the HERA dish is 75 mm at 200 MHz. However, inclusion of a 'sag' on the panels delivers a comfortable RMS value of 12 mm.

Another merit of the performance of a reflector antenna is the aperture efficiency as discussed in Chapter 2.2. By using Equation 2.2.1 we can show that the taper angle for HERA is

$$\theta_0 \approx 76^\circ \, .$$

If $n = 2$ in Equation 2.2.4 then the aperture efficiency for the HERA dish according to Equation 2.2.5 should be approximately 77%. However, this is assuming an ideal feed pattern as shown in Figure 4.8, while it can be shown that the PAPER feed does not perform nearly well enough to be approximated by $n = 2$.

This is also implied by the illumination results in Figure 4.6 implying that a poor efficiency is expected. Shown in Figure 4.9 is the aperture efficiency

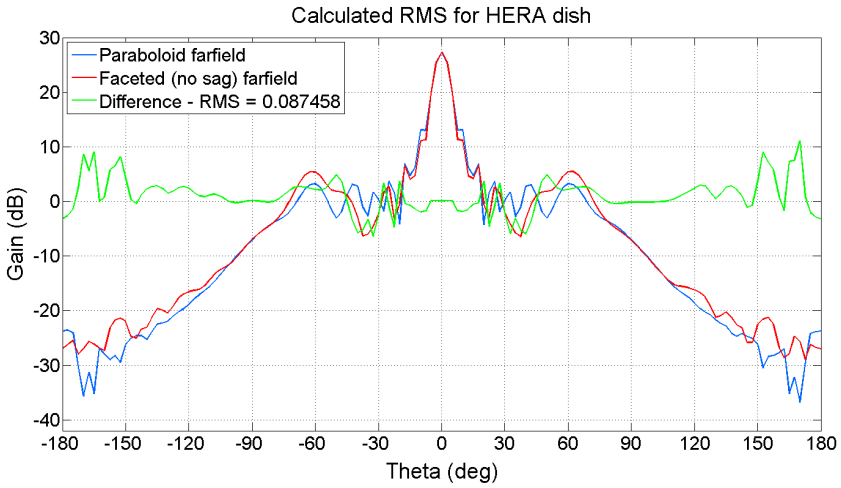

Figure 4.7: Farfields of a perfect paraboloid (blue), the faceted HERA dish with 'sag' incorporated into the panels (red) and the difference between the two fields (green).

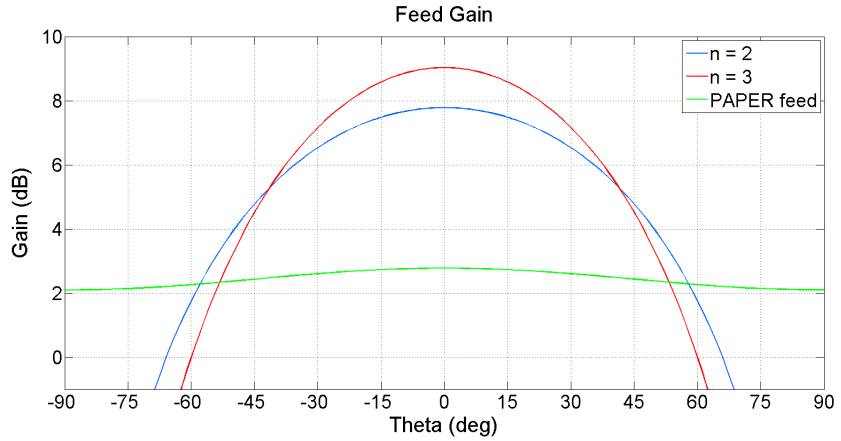

Figure 4.8: Feed gain at $\phi = 0°$ for two cases of ideal feeds compared to the weaker PAPER feed.

calculations based on the FEKO gain shown in Figure 4.2. The reflector efficiency is very weak across the whole band. The efficiencies fall far under the standards for a parabolic reflector which indicates that it is a poor feed according to expected standards.

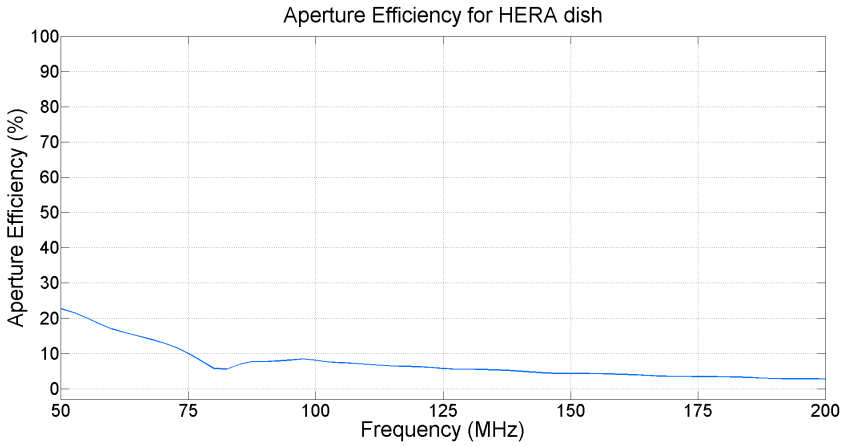

Figure 4.9: HERA dish aperture efficiency with the PAPER feed at a focal length of 4.5 m.

4.4 HERA as an Interferometer

4.4.1 Configuration and uv-coverage

This section investigates HERA not only as a single dish, but as an array of dishes. The configuration of an interferometer is determined by the science it will be used for and since hydrogen is detectable as large structures in the sky, the ideal configuration for HERA would be tight packed elements. This is realised in a hexagon-shaped configuration where the minimum spacing between the elements optimizes the baseline for large structures in the sky. However, this grid configuration will give bad coverage of the uv-plane, which implies that HERA 331 will not be a good imaging telescope. This can be shown by plotting the uv-coverage for 331 packed HERA elements using script computed by the author in MATLAB. A single observation of the uv-plane containing $N_{bases} = 54615$ baselines is shown in Figure 4.10 where the latitude is $\mathcal{L} = -30.72°$ and the declination is $\delta = -25°$. To improve the uv-coverage, some outlying antennas can be included. The uv-coverage of these are shown in Figure 4.11. The longer baselines dramatically improve the imaging capabilities of the interferometer and allow for small-scale structures to be detected.

However, the aim of HERA is not to make an image but rather a measurement of a particularly point in the uv-plane by sampling the same point repeatedly. Every pair of antennas with the same baseline and direction measures the same signal regardless of its location. Figure 4.12 shows HERA 331 and HERA 350 for 12 hours of observation. The improvement in uv-coverage for HERA 350 is evident.

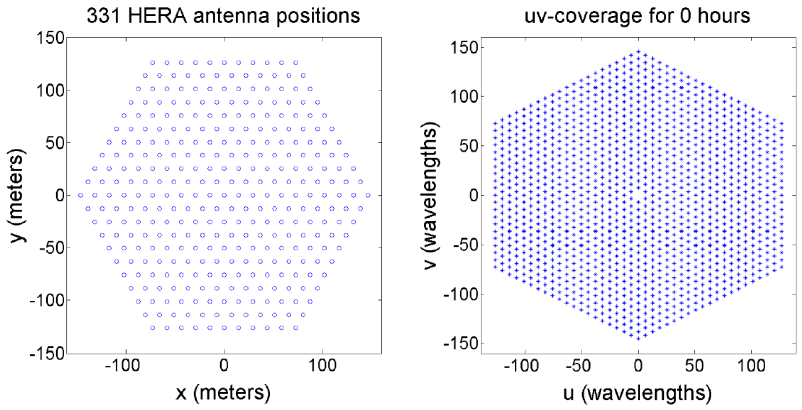

Figure 4.10: The location of 331 HERA elements (left) and the single observation *uv*-coverage (right) with inter-antenna spacing of 14.6 m.

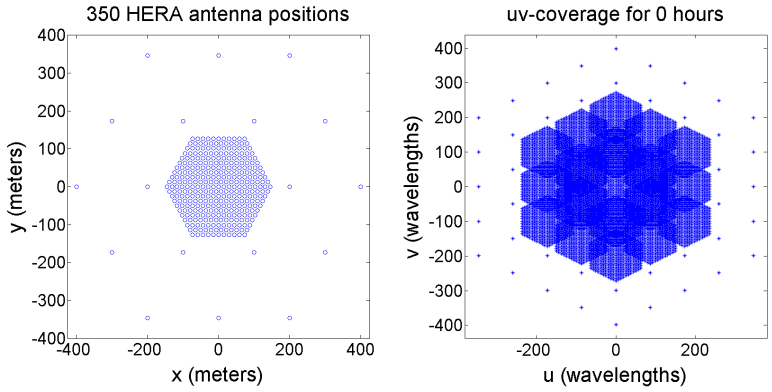

Figure 4.11: A plot showing the location of 350 HERA elements (left) and the single observation *uv*-coverage (right).

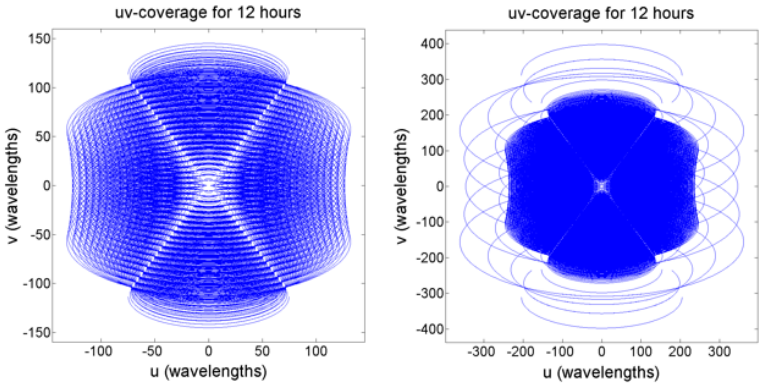

Figure 4.12: A plot showing the *uv*-coverage for 12 hours of observation for HERA 331 (left) and HERA 350 (right) which includes outlier elements.

The wavelength at 150 MHz is $\lambda = 2$ m and for $N_{ant} = 350$ and $N_{bases} = 61075$ the minimum and maximum baseline length is 14.6 m and 800 m, respectively. This delivers the following interferometry parameters,

$$\begin{aligned} \delta\theta &\approx 0.143^\circ \\ \theta_{max} &\approx 7.85^\circ \\ \theta_{FoV} &\approx 8.19^\circ \, . \end{aligned}$$

4.4.2 Reflections in Delay-space

The delay-spectrum technique is presented in Chapter 2.4 as a method used by HERA astronomers to separate signals such as the EoR from brighter foreground emissions. Having this knowledge it is evident that in its simplest form HERA aims to measure a signal which is rapidly varying (ones and zeroes) representing the spectrum of hydrogen. The EoR signal can be concealed by variations in the frequency response of the antenna element by allowing foregrounds into the EoR window, which are found beyond the baseline length. Hence, to guarantee that an antenna instrument will be able to detect the EoR signal, it should be designed so that all spectral structure is within a specific region of delay-space.

For the above-mentioned to work, it is important to incorporate reflections caused by the antenna element itself. In [24] it is shown that fixing a specification on the reflections of a dish is the same as fixing a specification on the smoothness of the voltage signal in the frequency domain. Consider if the interferometer receives a signal which is initially very smooth and would therefore be found at a low delay. By multiplying this spectrum times a rapidly varying function of frequency would cause a FT to deliver misplaced power spilling over into higher delays.

For this reason it is important to design HERA without internal reflections that has certain power within a specified delay. The derivation of these values is outlined in [23] where it is assumed that the antenna pattern A and the sky intensity I in Equation 2.3.14 are both uniform or perfectly flat functions of frequency. In the delay space this would imply two delta functions centered at zero delay $\tau \approx 0$. It is also shown in [23] that these smooth signals are approximately five times brighter than the EoR signals. Securing a safe relationship between the two signals gives

$$\frac{|\langle \tilde{A} * \tilde{I} \rangle(\tau)|}{|\langle \tilde{I} \rangle(\tau = 0)|} < 10^{-6} \, (-60 \text{ dB}) \, , \tag{4.4.1}$$

where $\tilde{}$ denotes Fourier transformation along the frequency axis and $\langle \bullet \rangle$ denotes the average over solid angle. Hence, the frequency dependent gain of the antenna is influenced by any reflections in the signal path creating ripples in sinusoidal form. Also, ripples at higher frequencies are caused by larger

delays. To prevent concealment of the EoR signal, the spectrum of the source in delay-space should have a response that is not greater than the length of the shortest baseline down by 60 dB relative to the response at $\tau = 0$. For HERA, the shortest baseline measured in light travel time is 14.6 meters which correlates to approximately 49 ns. A sligthly less stringent specification would be where reflections are no higher than -60 dB after 60 ns. In mathematical form this is written as

$$\frac{|\langle \tilde{A} \rangle(\tau = 60\,\text{ns}, \mathbf{s})|}{|\langle \tilde{A} \rangle(\tau = 0\,\text{ns}, \mathbf{s})|} < 10^{-6}\,(-60\,\text{dB})\,. \tag{4.4.2}$$

This specification can be evaluated by data obtained from EM simulations. This process is oulined in [25] and next implemented here. The reflection data is obtained by dividing the output signal v_{out} of a port by the input signal v_{in} of the same port which, in this case, is a result of a full-wave time-domain simulation in CST (Richard Bradley collaborative unpublished). Figure 4.13 show the input and output signals for a 500 ns simulation. The input signal reflects against the dish and reaches the feed again 9 meters or, in free space, 30 ns after excitation. The ripples between 60 ns and 80 ns of the output signal hence represents waves which have reflected against the dish. For the remainder of this work, this reflection is called the secondary reflection.

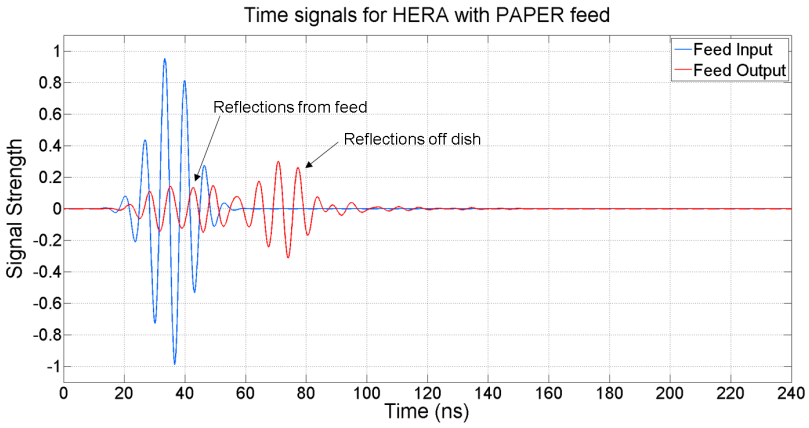

Figure 4.13: Input and output signals from a 500 ns CST time-domain simulation.

Figure 4.14 shows the voltage signals on a dB scale with both signals shifted to the left by approximately 30 ns to compensate for the delay before the maximum point of excitation. The input signal is also normalized at $t = 0$. When observing the raw output signal it is clear that it does not meet the -60 dB at 60 ns specification as indicated by the dashed lines. Rather, the signal is measured at -28 dB after 60 ns.

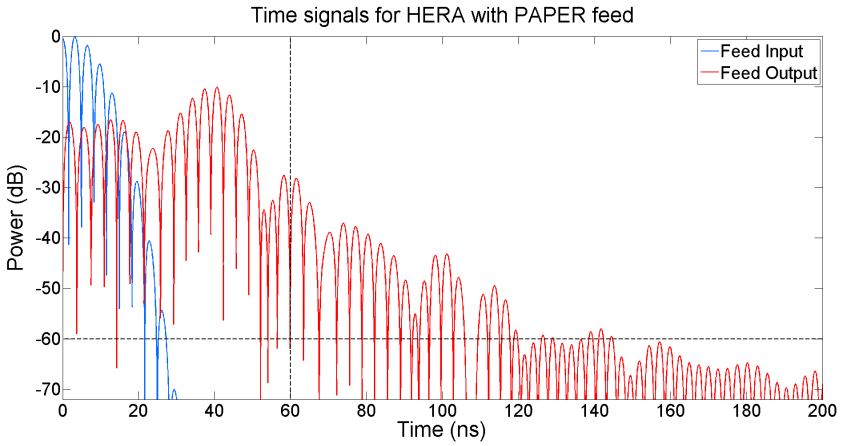

Figure 4.14: Feed input and output signals from a CST time-domain simulation showing that the dish does not meet the -60 dB by 60 ns specification. Instead, the output or reflection is approximately -28 dB at 60 ns.

However, even though the reflectrometry of the dish does not pass the specification, the signal path does not end at the feed. If $\tilde{R}$ is the FT of the response function the following is true for the output signal

$$\tilde{v}_{out}(\omega) = \tilde{R}(\omega)\tilde{v}_{in}(\omega)\ . \tag{4.4.3}$$

Recognizing the convolution theorem from Equation 2.3.4 on the right side of Equation 4.4.3 shows that the output signal can be obtained by the convolution of the antenna response function and the antenna input signal

$$v_{out}(t) = \int R(\tau)v_{in}(t-\tau)\,d\tau\ . \tag{4.4.4}$$

Figure 4.15 shows, amongst others, the spectrum of both the input and output signals as well as the response function within a 10 GHz limit.

Next, the response function is multiplied by a Blackman-Harris window in the frequency domain as also shown in Figure 4.15. Even though in the time-domain this simulates a low-pass filter, the motivation is to suppress the foreground sidelobes in the delay domain when convolved with the response. Alternatively, using a top-hat window in the frequency domain causes a smearing of the foreground sidelobes over all of delay space, concealing the EoR signal. However, the sidelobe suppression delivered by a Blackman-Harris window is sufficient to make most of the large delays foreground free. The window is centered at 150 MHz and set to zero outside of between 50 MHz and 250 MHz [24] seeing as the correlator on HERA also limits the signal to a finite bandwidth. After applying the filtering step $\tilde{F}$, the response in the frequency domain is

$$\tilde{v}_{out}(\omega) = \tilde{R}(\omega)\tilde{v}_{in}(\omega)\tilde{F}(\omega)\ . \tag{4.4.5}$$

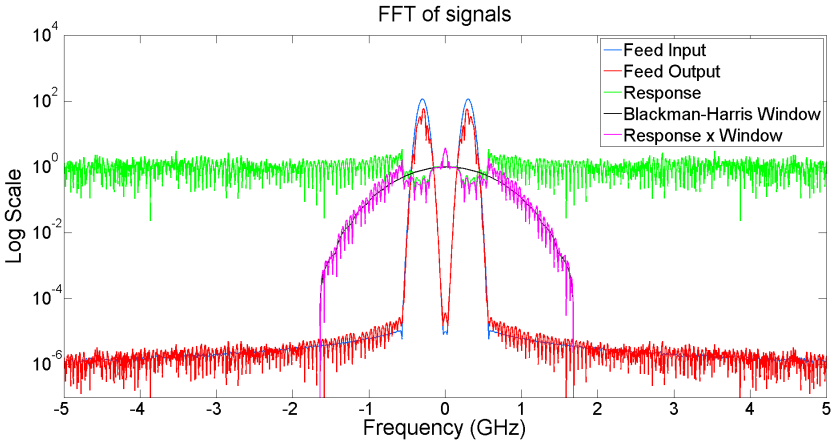

Figure 4.15: The FFT of the feed input, feed output, the response function, the Blackman-Harris window and the response multiplied by the window.

Finally, working backwards from the response function, the filtered output signal can be obtained. The signal as a function of time is obtained by applying an inverse Fourier Transform. The feed input and windowed feed output is hence shown in Figure 4.16 where the Blackman-Harris window cause approximately a 4 dB decrease in the output signal. This results in a reflection of -35 dB at -60 ns. This shows that any spectral structure introduced by reflections adds the foregrounds to higher delays so that even if the sidelobes of low delay foregrounds are suppressed, there will be foregrounds at high delays due to the intrinsic spectral structure of the antenna.

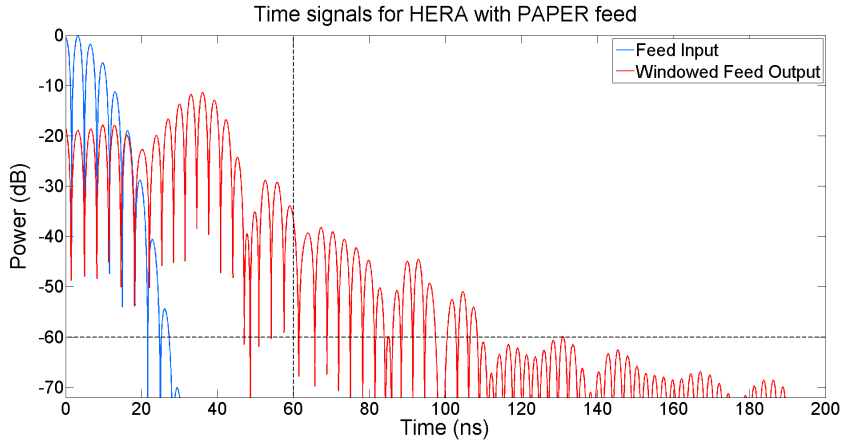

Figure 4.16: Feed input and windowed output signals from a CST time-domain simulation. The output signal or reflection is approximately -35 dB at 60 ns.

4.4.3 Mutual Coupling

It is important to keep mutual coupling in a low frequency array to a minimum, because of the faint radio signals being observed. However, this can be a difficult task because of the wider FoV at these frequencies. Also, HERA is a closely packed array which implies that extra measures had to be taken to prevent mutual coupling. In the original design this need is met in the form of a screen around the edge of the dish as previously seen in Figure 4.1. However, as seen in Figure 4.2 the shortcomings of this design is evident. Figure 4.17 shows an array modelled in FEKO of seven HERA faceted dishes with the PAPER feed and the dish screen excluded.

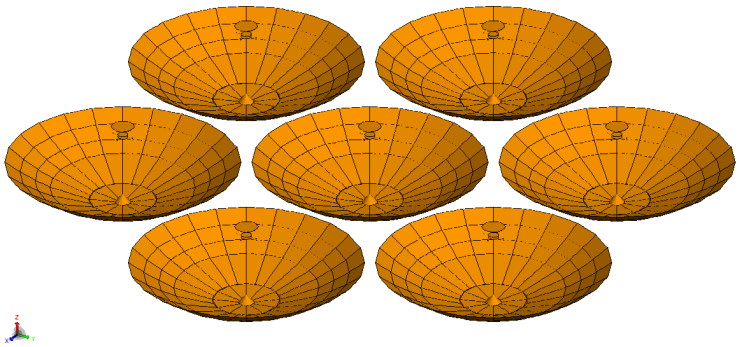

Figure 4.17: Seven HERA dishes without the screen and separated by 60 cm.

To assess the mutual coupling between the elements a 50 Ohm load is added on each x-polarized (or uneven numbered) port. Shown in Figure 4.18 is a comparison of the S32 and S42 parameters when the screen is both included and excluded. S32 and S42 represents X-pol and co-pol coupling, respectively. As expected, the X-pol coupling is significantly less than the co-pol coupling. It is shown that the effect of the screen might also be negligible as there is no prominent difference in the comparison. Also, the increased structure across frequency caused by the screen is yet again noticeable. Figure 4.19 shows a radial gain plot of the array with and without screen at 150 MHz. An increase in backlobe gain is visible if the screen is removed indicating some spillover.

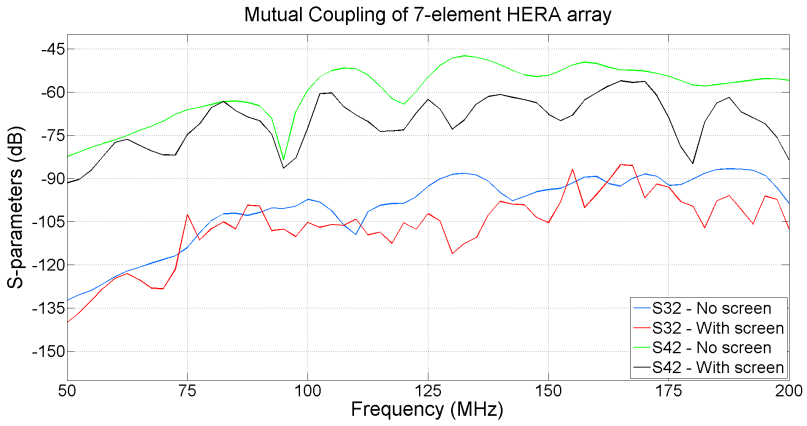

Figure 4.18: The S32 and S42 parameter of a 7-element packed HERA array both with and without the screen.

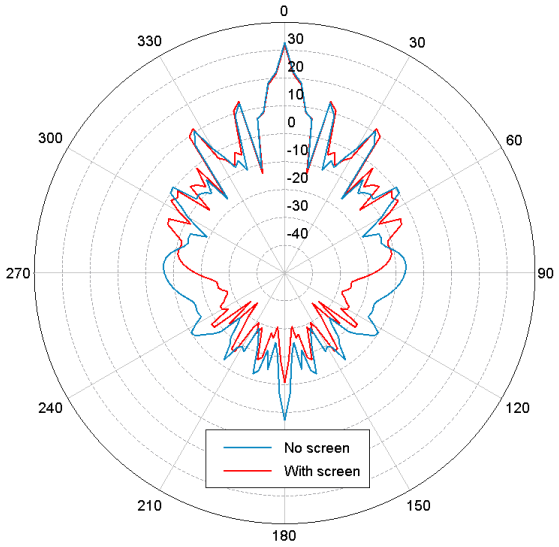

Figure 4.19: Radial gain resuls at $\phi = 0$ and a frequency of 150 MHz for a 7-element HERA array for the case of with and without screen.

4.5 Conclusion

In this section HERA was analysed as a single element and as an interferometer. It is shown that HERA 352 intends to be capable of accurate power measurements as well as excellent imaging capabilities. The inherent reflection properties of the HERA dish prevent the accurate use of the delay-spectrum technique to isolate foregrounds. In the next section modelling and EM analysis of different feeds for HERA are investigated.

Chapter 5

Design and Implementation of Feeds for HERA

5.1 Introduction

The current HERA feed consists of the PAPER crossed sleeved dipoles which has the advantage of producing very smooth gain, but are not by nature very wideband. Hence, alternative feeds are also investigated in this thesis both for the operating band and the lower band from $60 - 120$ MHz. This chapter begins by discussing the specifications for the HERA feeds.

5.2 Feed Specifications

The first obvious specification of a feed for HERA is the ability to operate over a bandwidth of 4:1 as the possibility of more than one feed on the same dish is not a practical option. Secondly, it is known that celestial sources emit E-fields and H-fields in unknown orientation which makes dual-polarized feeds a non-negotiable specification for the HERA feeds. The feeds must also be able to operate at the mentioned low frequencies with large wavelengths in the range of $\lambda = 1.5 - 6$ m. Furthermore, these wavelengths will force the dish to in effect operate more as a backplane than a reflector. The FEKO models for all feeds were ideally and differentially fed by thin wires at the crossing of the dual-elements.

5.3 PAPER

The Precision Array for Probing the Epoch of Reionization is a $100 - 200$ MHz array [26] located at the Murchison Radio Observatory (MRO) in Western Australia and in the Karoo in South Africa. A prototype station is also located at NRAO in Green Bank, West Virginia as shown in Figure 5.1. As a

predecessor to HERA, the goal is similarly to detect 21 cm emission from the early universe [26].

Figure 5.1: PAPER prototype elements at Green Bank, West Virginia, USA.

PAPER elements are dual-polarized, sleeved dipoles mounted above grounding structures (including side reflectors). A dipole antenna can also be called a sleeve antenna or dipole when the exterior of the coaxial transmission feed line is used as a radiating element. It is different from a conventional base-driven half-dipole (monopole) over a conducting ground plane in that the sheath of the coaxial line does not end at the ground plane but extends above it as shown in Figure 5.2.

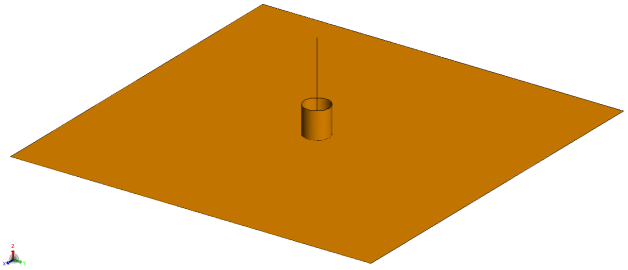

Figure 5.2: A sleeved monopole above a conducting ground plane as modelled in FEKO where the excitation is placed between the wire and ground.

It is known that a sleeve antenna can be operated over a much wider bandwidth than a thin conventional dipole antenna. To observe the effects of a sleeve on a dipole or monopole, a monopole over a conducting plane similar to the one described in [27] was modelled in FEKO. As seen in Figure 5.3 the sleeved antenna resonates at two frequencies in the lower band compared to the one resonance of the normal monopole. The reflection coefficient results in Figure 5.4 show that the sleeved antenna is better matched overall across the band. Also, the VSWR results is shown in Figure 5.5 and although the VSWR of the sleeved antenna is still undesirable, there is an improvement compared to the sleeveless antenna.

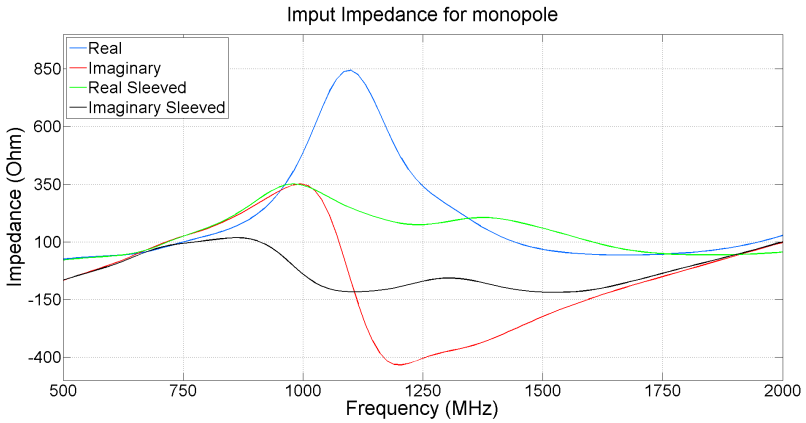

Figure 5.3: The input impedance of a normal and sleeved monopole above a conducting ground plane.

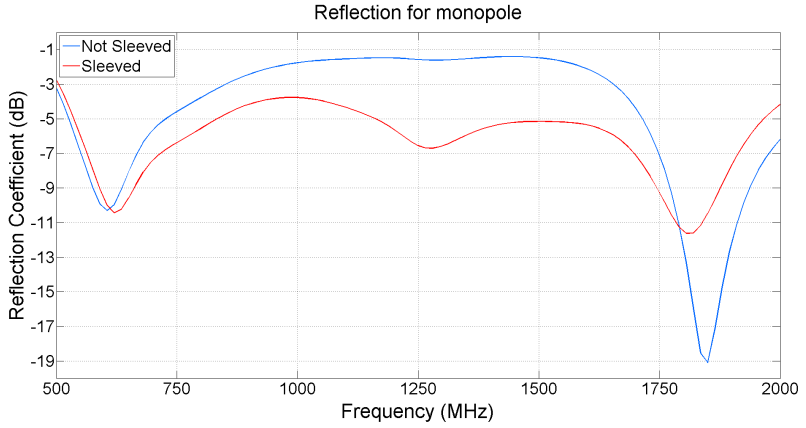

Figure 5.4: The reflection coefficient of a normal and sleeved monopole above a conducting ground plane.

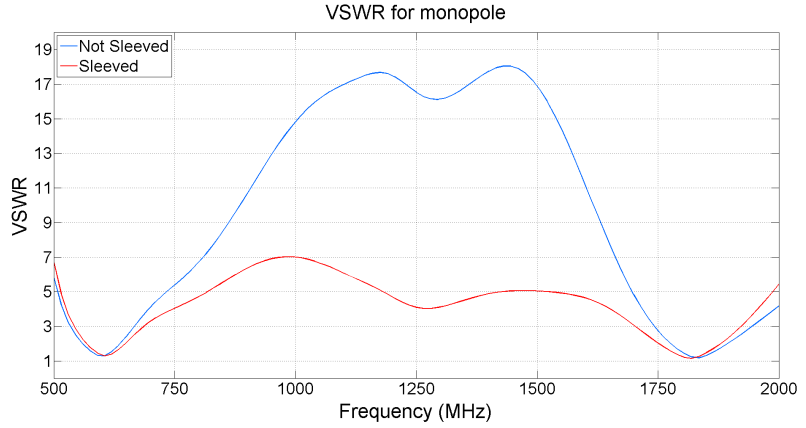

Figure 5.5: The VSWR of a normal and sleeved monopole above a conducting ground plane.

Having seen the effect of a sleeve on a radiating element, the PAPER element is next investigated. This element has the combined advantage of the cost-effectiveness of the dipole and the ruggedness of the sleeved dipole. The dipoles also produce a desired spatially smooth primary beam pattern that evolves slowly with frequency. The design in FEKO shown in Figure 5.6 includes the grounding structures as well as the half-wave crossed dipoles covered by two disks that act as the sleeves. Because the actual amplifier is housed within the mast lifting the dipoles above the ground screen, the excitation in the FEKO model was placed at the point where the dipoles cross. This is also the case for all succeeding feeds investigated in this thesis.

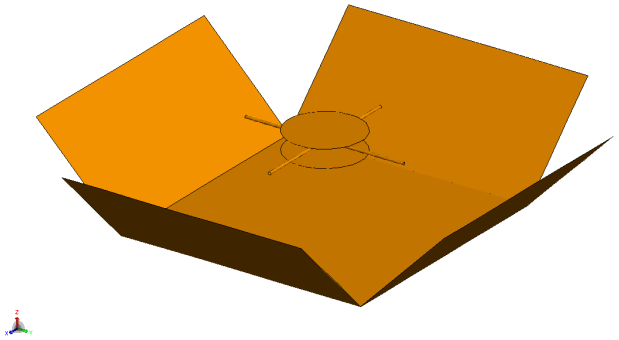

Figure 5.6: 3D view of the PAPER antenna element as modelled in FEKO.

To illustrate the effect of the side-reflectors the PAPER element were initially modelled without the side reflectors. The remaining design then includes the 1.32 meter half-wave crossed dipoles, the 0.305 radius sleeves and a 2×2 meter ground plane. At 150 MHz the gain achieved for this design is 5.9 dB with a HPBW of 71°. As expected, with the addition of the side-reflectors at an angle of 45° the gain improved to 11.3 dB and the HPBW narrowed to 43.2°. The zenith gain at 100 MHz, 150 MHz and 200 MHz is shown in Figure 5.7.

The input impedance is shown in Figure 5.8. There is a single resonance within the $100 - 200$ MHz range at 107 MHz. The reflection for PAPER referenced to 125 Ohm is shown in Figure 5.9 and delivers an operating band at -10 dB of $105 - 180$ MHz.

Optimization for the PAPER element included alternating the height of the dipoles above the ground plane, the radius of the sleeves and the distance between the sleeves and the dipoles. By running Genetic Algorithm optimizations in FEKO, it was found that the original design is at optimum. An increase in the distance between the sleeves and the dipoles caused smaller bandwidth which supports the case for the sleeves. Results also show that a broad bandwidth is achieved with a disc radius of approximately a quarter wavelength or less.

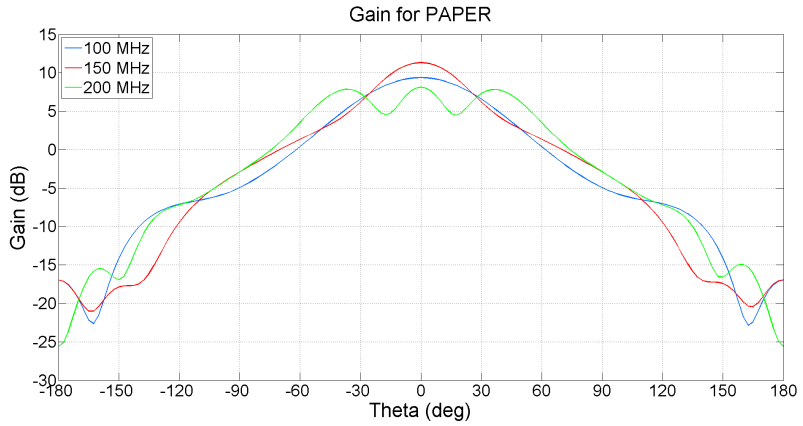

Figure 5.7: Gain of the PAPER antenna element at 100 MHz, 150 MHz and 200 MHz.

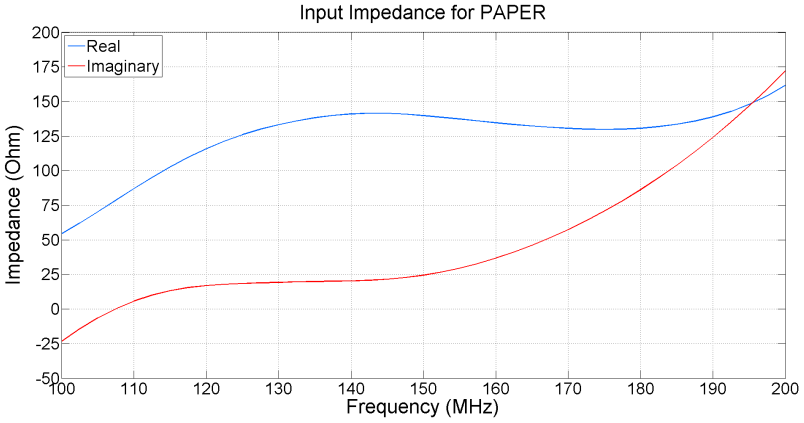

Figure 5.8: FEKO input impedance of the PAPER antenna element.

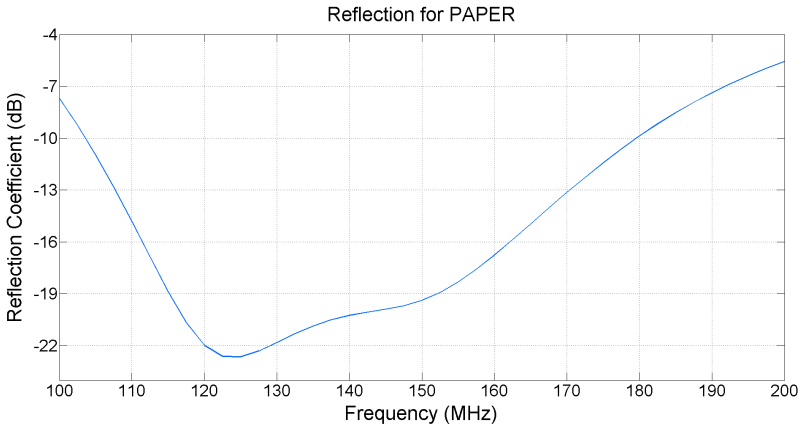

Figure 5.9: FEKO reflection coefficient of the PAPER antenna element referenced to 125 Ohm.

Having investigated PAPER as the current HERA feed, it is possible to now further investigate alternative feeds for improved performance. These are investigated in the following section where all feeds are compared to the PAPER feed without the grounding structure.

5.4 Alternative Feeds

5.4.1 Bowtie Feed

The first alternative feed investigated was the bowtie feed. This feed operates the same as the dipole, except that the wider angle makes for wider bandwidth. Bowtie antennas are the planar cross-sections of biconical antennas and consist of two triangular metal sheets [28]. Their radiation pattern are similar to those of a simple dipole, but performance is limited below 30 MHz because of the dipole's radiation characteristics [29]. Biconical antennas have poor efficiency at low frequencies, resulting in low field strengths when compared to the input power [28]. Figure 5.10 shows a FEKO model of two bowties with the PAPER sleeves. This was the starting point of the optimization process.

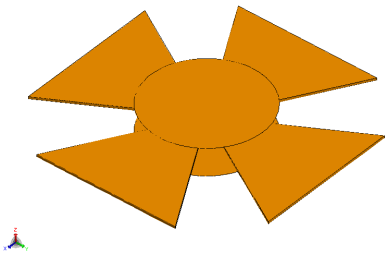

Figure 5.10: A dual-bowtie feed with the PAPER sleeves as modelled in FEKO.

Optimization of the following parameters where investigated. The wide-angle, the length and the thickness of the bowtie as well as the radius and the gap of the sleeves or discs. It was found that there is a constant trade-off between gain in higher frequencies and -10 dB bandwidth where the angle of the bowtie is the major determining parameter. Figure 5.11 and Figure 5.12 shows respectively the reflection and gain of the bowtie feed compared to PAPER for three different angles.

From these figures it can be observed that as the angle and bandwidth increase the gain also drops dramatically at the higher end of the band. Further conclusions are that the thickness of the bowtie should not be smaller than 0.01 meter for the sake of reflection in higher frequencies. The radius of the sleeves also should not be more than 0.3 meters for sake of smoothness across frequency. Rounding the sharp corners of the bowtie has the effect of less variation in reflection across the band. The bigger the radius of the corners, the better the gain at the higher frequencies for all angles. Figure 5.13 shows

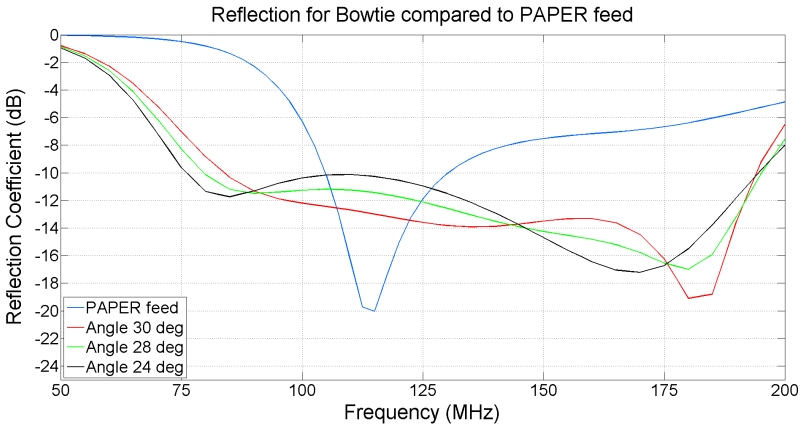

Figure 5.11: Reflection referenced to 75 Ohm of the Bowtie feed for three angles compared to the PAPER feed.

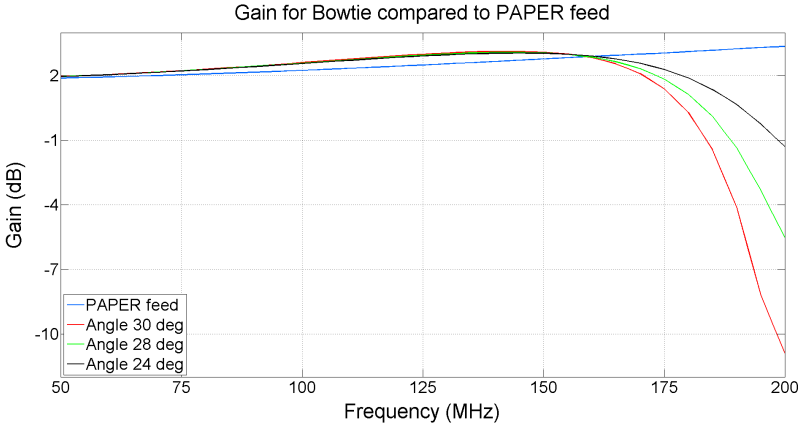

Figure 5.12: Gain of the Bowtie feed for three angles compared to the PAPER feed.

the bowtie feed with an angle of 30° with currents at 200 MHz for one excited port. Here it can be observed that the reason for the decline in gain at these frequencies is due to extra modes being generated on the orthogonal feed. This causes a cancellation in gain. It is found that the gain starts decreasing at an optimal angle of 16°. Figure 5.13 shows this optimal bowtie where the feed works at higher frequencies.

Also, Figure 5.14 shows the port-to-port S21 parameter for both feeds where port 2 is loaded with a 50 Ohm load. It can be observed that for both the wide and optimized bowtie, the coupling is not significant.

Several modifications were investigated for the wide bandwidth to keep the antenna working even in the higher frequencies. These include punching a hole in the middle of the bowtie where the size and shape were also investigated. The results however did not improve significantly due to most of the currents flowing on the rim of the bowtie and not in the center. Making corrugations in the bowtie resulted in less bandwidth as in effect the bowtie width decreases.

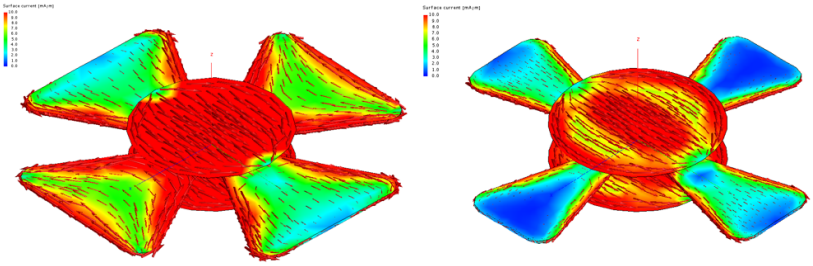

Figure 5.13: The currents at 200 MHz for a bowtie with a wide angle (left) and an optimized angle (right). Extra modes form on the wide bowtie which causes a decrease in gain.

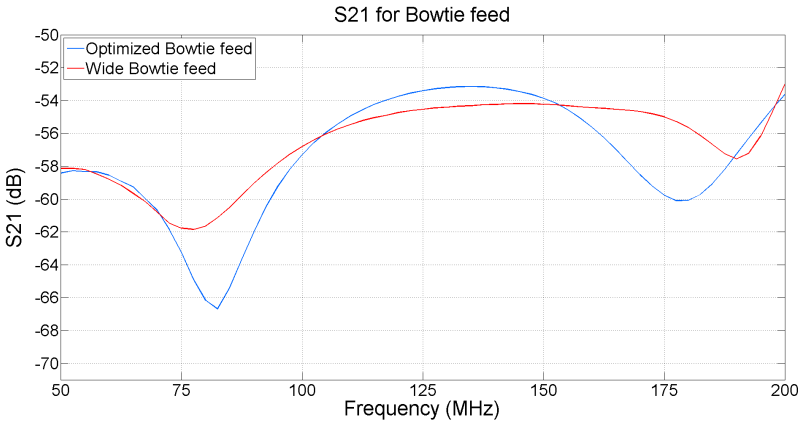

Figure 5.14: The S21 parameter for the wide and optimized bowtie feed.

Figure 5.15 shows the gain of the optimized bowtie feed compared to the PAPER feed. There is no significant difference in the magnitude and the gain of the bowtie only decreases after 200 MHz. Figure 5.16 shows the reflection where the PAPER feed is referenced to 125 Ohm and the Bowtie feed to 75 Ohm. The bowtie feed has a greater bandwidth extended towards the lower frequencies.

One modification which showed promising results was to indent the bowtie in the mid-section of each arm as shown in Figure 5.17. A case for sharp and round corners were investigated. This modification was done based on several literature sources which show that similar modifications improve the bandwidth of the bowtie [30].

The gain of these modified bowtie feeds compared to the PAPER feed and the optimized bowtie feed is shown in Figure 5.18. As the gain of the optimized bowtie feed starts dipping, the modified feeds seem maintain their gain better. The reflection is shown in Figure 5.19 where the modified bowtie with sharp corners display a deep reflection with a decent bandwidth. The modified bowtie surprisingly does not perform as well with round corners.

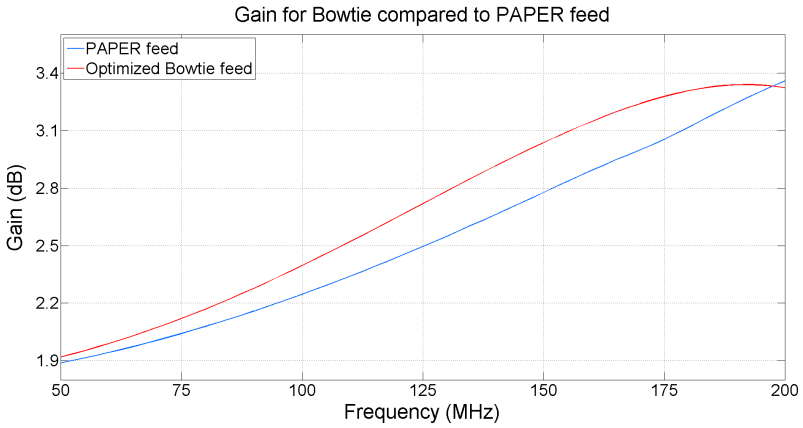

Figure 5.15: Reflection referenced to 75 Ohm of the optimized Bowtie feed compared to the PAPER feed.

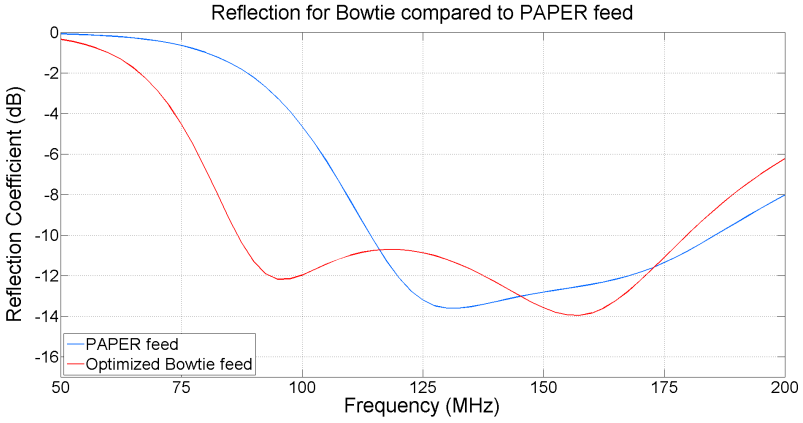

Figure 5.16: Gain referenced to 75 Ohm of the optimized Bowtie feed compared to the PAPER feed referenced to 125 Ohm.

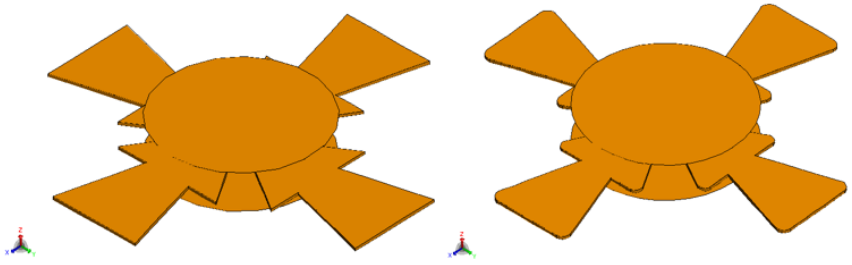

Figure 5.17: A bowtie feed modified by indenting the mid-section of each arm. Sharp (left) and round (right) corners were investigated.

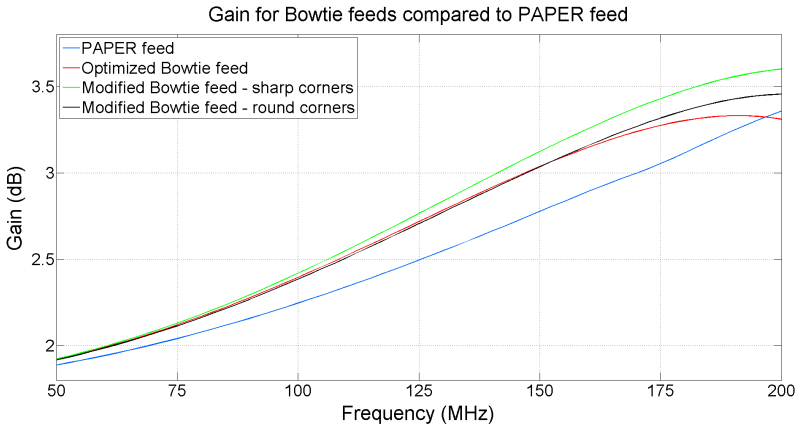

Figure 5.18: The gain of several versions of the bowtie feed compared to the PAPER feed.

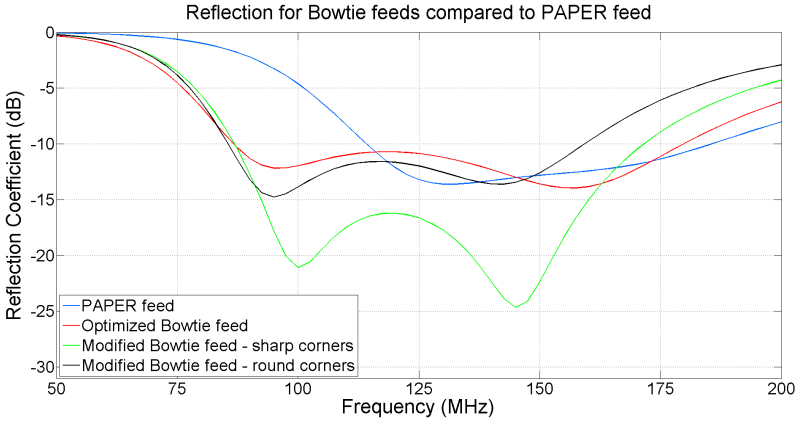

Figure 5.19: Reflection of several versions of the bowtie feed compared to the PAPER feed. PAPER referenced to 125 Ohm, the optimized bowtie feed referenced to 75 Ohm and the modified feeds referenced to 50 Ohm.

5.4.2 Low Frequency Scaled PAPER Feed

From the PAPER and Bowtie feed it is evident that the operating bandwidth is restricted to approximately 100-200 MHz. However, there is also important science below 100 MHz and for this reason an up-scaled PAPER feed was investigated. It is intended that a small part of the array be equipped with the low frequency feed. Some challenges were faced in this implementation due to the size of the dipoles at such low frequencies. If the dipoles were to have a centre frequency of approximately 60 MHz, the corresponding dipole length would be 2.6 meters. In addition to the larger dipoles and sleeves a wire mesh cylinder is also included to decrease the edge effect of the dipoles. The edge effect causes waves to travel back towards the port because of an abrupt cut-off at the end of the physical feed. However, the cylinder increases

structure in the gain measurements, much the same as the screen around the HERA dish. The FEKO model for the scaled version is shown in Figure 5.20.

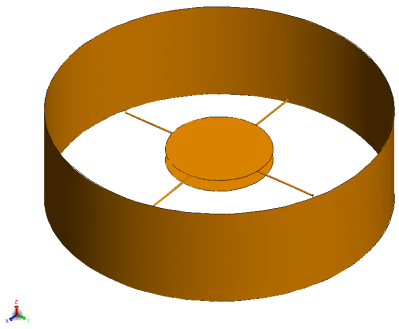

Figure 5.20: A FEKO model of the scaled up version of the PAPER feed for frequencies below 120 MHz.

As with the bowtie feed, the scaled PAPER feed is next compared to the normal PAPER feed. The zenith gain is shown in Figure 5.21 where the scaled feed impresses with high gain up to 120 MHz which is sufficient since this feed is only to be used at the lower frequency range.

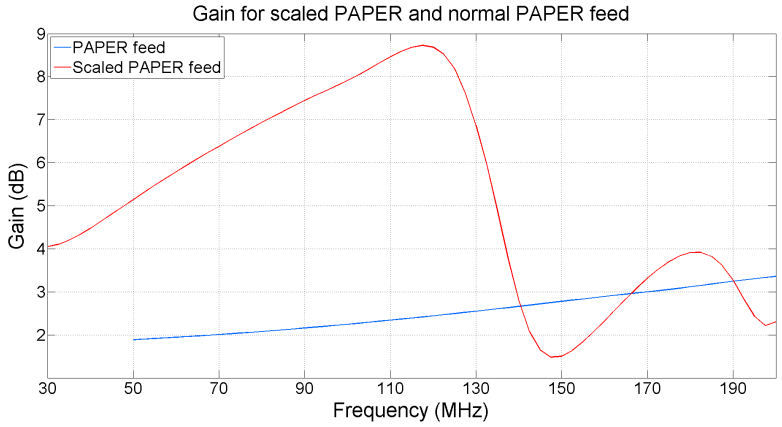

Figure 5.21: Zenith gain of the scaled PAPER feed compared to the normal PAPER feed.

Investigating the feed further, shown in Figure 5.22 and Figure 5.23 is the input impedance and the reflection compared to PAPER, respectively. The reflection coefficient for PAPER is once again referenced to 125 Ohms where the scaled feed is referenced to 160 Ohms. The scaled feed resonates as expected at approximately 60 MHz which causes the -10 dB bandwidth at the lower frequencies.

Positioning this feed above the HERA dish introduces some mechanical constraints as the larger feed implies a larger backplane. Due to this some aperture blockage would be expected which could decrease the sensitivity of

the array. Another mechanical constraint is the weight of the feed as it is held aloft by three wires. The total weight of the scaled up PAPER feed is calculated to be approximately 125 kg (276 lbs).

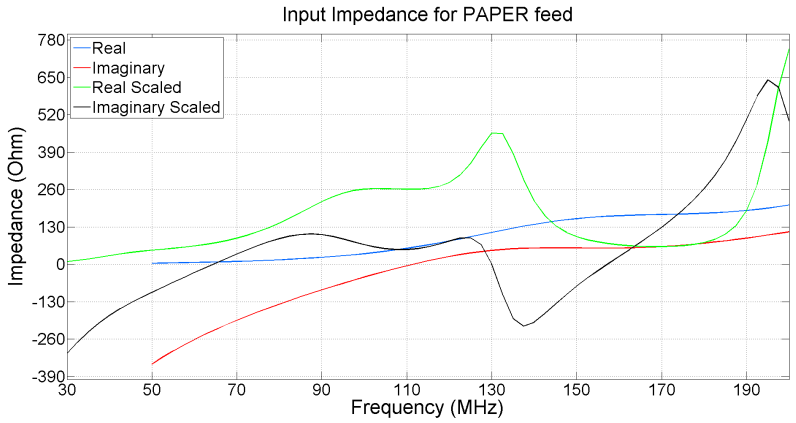

Figure 5.22: Input impedance of the scaled PAPER feed compared to the normal PAPER feed.

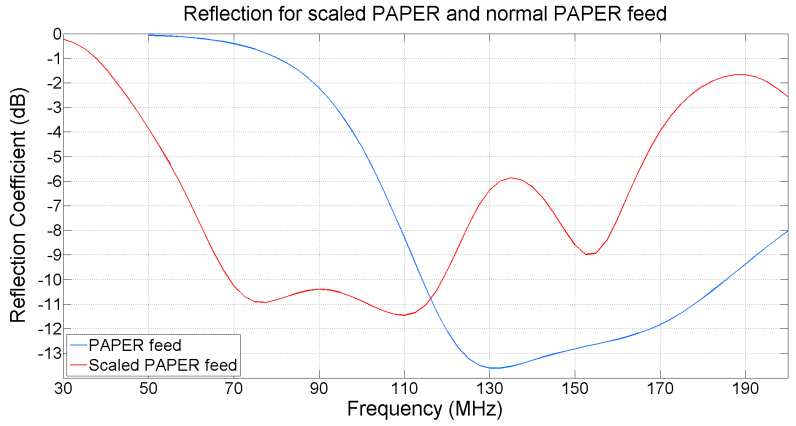

Figure 5.23: Reflection of the scaled PAPER feed referenced to 160 Ohm compared to the normal PAPER feed referenced to 125 Ohm.

5.4.3 Planar Sinuous Feed

Considering the previous feeds investigated in this section, further research was taken into even wider bandwidth, dual-polarized feeds. By ignoring the challenge of size for a moment and focusing on the electrical specifications, a planar sinuous feed can also be investigated as a possible feed for HERA. In this application the sinuous antenna consists of dual two-arm curves with two orthogonal polarizations. Furthermore, the angular width, growth rate and rotation angle is selected, respectively, as

$$\alpha_p = 45^\circ$$
$$\tau_p = 0.65$$
$$\delta_p = 22.5^\circ \, .$$

By choosing these parameters such as to achieve a self-complementary antenna, the input impedance is constant at $R_m = 133$ Ohm at a two-arm terminal and approximately 267 Ohm for the whole system. The outer diameter of the sinuous feed is approximately 4 meters to obtain a minimum frequency of 50 MHz. The inner feed diameter is 0.45 m which delivers a bandwidth of more than 10:1. A FEKO model of the sinuous feed is shown in Figure 5.24 with the outer and inner radius defined as

$$R_L = 2 \text{ m}$$
$$R_H = 0.225\text{m} \, .$$

Figure 5.24: A FEKO model of the planar sinuous feed with a bandwidth of 50 MHz to 300 MHz.

The gain of the sinuous feed for $30 - 1130$ MHz is shown in Figure 5.25. There is approximately 2 dB variation in the gain and on average almost 4 dB increased gain compared to the PAPER feed. The input impedance and reflection coefficient is shown in Figure 5.26 and Figure 5.27, respectively. The reflection coefficient shows very promising results with an operating band of 1 GHz covering $50 - 1050$ MHz.

Optimization in FEKO was also performed on the sinuous antenna. The inner diameter was decreased for the final design to add more cycles to the curve toward the center terminals. This has the effect of a reduce in discontinuity. An increase in the angular width resulted in large variations in gain, which is undesirable. To maintain the constant input impedance across the band, the rotation angle was not varied.

As an exception to the rule, the sinuous antenna was scaled, manufactured and measured which contributes to a more practical side of the thesis. This process is next described as well as results presented.

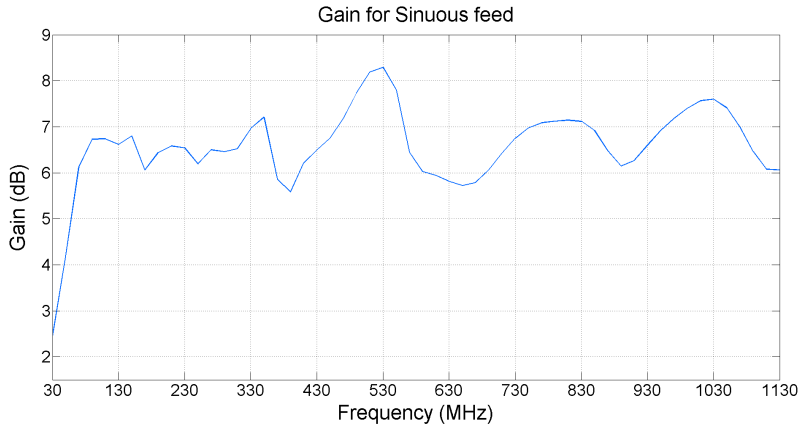

Figure 5.25: Zenith gain of the sinuous feed.

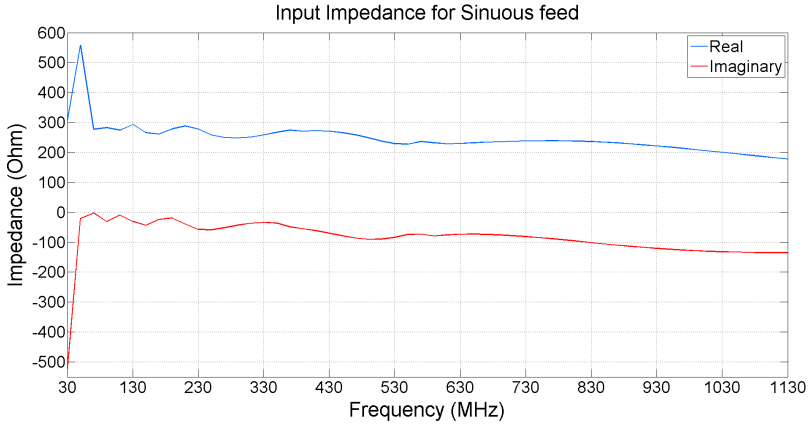

Figure 5.26: Input impedance for the sinuous feed.

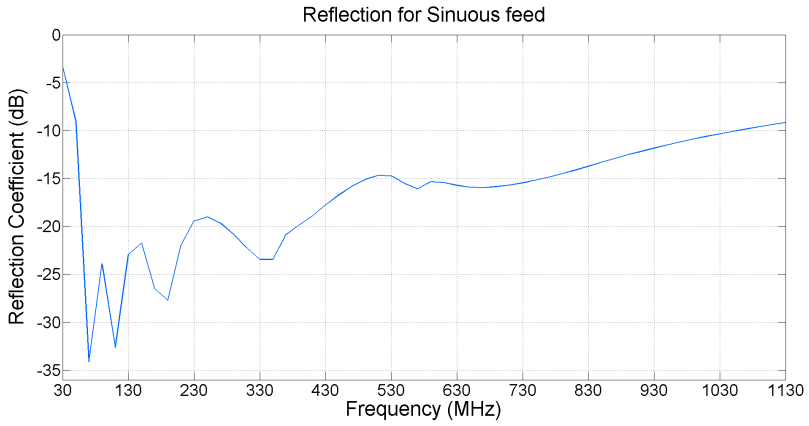

Figure 5.27: Reflection of the sinuous feed referenced to 267 Ohm.

Manufacturing and Measurements

The sinuous antenna presented in this section was scaled by approximately 41 times to obtain new dimensions for manufacturing which results in a shift in frequencies. The reason for this is two-fold. Firstly, the university's anechoic chamber can not accommodate frequencies as low as 200 MHz. Secondly, the cutting of the sinuous curve onto a substrate is limited to a certain size. The scaled dimensions are:

$$R_L = 0.0475 \text{ m}$$
$$R_H = 0.005\text{m} \, .$$

This scaling shifts the operating frequencies to approximately $2 - 41$ GHz. However, since there is only an interest in a 4:1 bandwidth as for HERA, the selected band is approximately $2 - 8$ GHz.

The design is based on [31] where the problem of the bi-directional radiation pattern of the sinuous feed is solved by using a ground plane under the planar sinuous antenna. However, this has the effect of cancelling the constant impedance resistance as calculated by Deschamp's equation. The sinuous antenna is designed on a Rogers R04003 substrate with a relative permittivity of $\varepsilon_r = 3.55$, a dielectric loss tangent $\tan\delta = 0.0027$ and a thickness of 0.508 mm. The size of the substrate is 115×115 mm. The height of the ground plane must be selected such as not to cause a null in the gain due to out of phase reflections at a specific frequency in the band. The height h can be calculated as

$$h = \frac{c}{4f} \, , \tag{5.4.1}$$

where

$$f > \frac{f_{max}}{2} \, . \tag{5.4.2}$$

With $f_{max} = 8$ GHz, a safe height would be below $h = 18.75$ mm. Hence, the height chosen for this design is 17 mm. Each arm is fed differentially with four thin wires running down to the ground plane. Also, between the feed and the ground plane, a cylinder of 8.5 mm height is placed around the wires to reduce radiation from the wires and to compensate for extra inductance. Finally, the wires are connected to etched out tapers (having the effect of a matching network) on the bottom of the back plane which terminates at four SMA connectors on each side. The manufactured design is shown in Figure 5.28.

The antenna patterns were measured in the anechoic chamber using a NSI 2000 system with spherical scanner and two different horn antennas as probes to obtain results over the whole band. The first probe is a broadband ridged

Figure 5.28: Top (left) and bottom (right) photographs of the manufactured sinuous feed.

guide and the second is a open ended waveguide used for 5.75 GHz and higher. Single-ended radiation patterns were measured and transformed to differential patterns using formulas obtained in [32]. The differential mode $\mathbf{E}_{dm}$ and common mode $\mathbf{E}_{cm}$ patterns are, respectively,

$$\mathbf{E}_{dm} = \frac{1}{\sqrt{2}}(\mathbf{E}_1 - \mathbf{E}_2)\,, \tag{5.4.3}$$

$$\mathbf{E}_{cm} = \frac{1}{\sqrt{2}}(\mathbf{E}_1 + \mathbf{E}_2)\,, \tag{5.4.4}$$

where $\mathbf{E}_1$ is the pattern obtained due to excitation at port 1 while port 2 is terminated in a matched load. The same is applicable vice versa for $\mathbf{E}_2$. The normalized $\phi = 0°$ radiation patterns for 3 GHz, 5 GHz and 7 GHz both measured and simulated is shown in Figure 5.29, 5.30 and 5.31, respectively. The FEKO model is fed at the bottom of the open cylinder and the effects of this can be seen in the higher backlobe of the simulated results. The measured main beam pattern displays a good roundness, except at higher frequencies were the gain starts decreasing at the zenith.

The S-parameters were measured using a Agilent PNA-X Network Analyser where all four ports were measured to obtain a complete single-ended S-parameter matrix. To transform the results to a mixed-mode matrix, the calculations in Appendix B.2 from [33] were applied. The mixed-mode S-parameters compared to simulated results are shown in Figure 5.32 where both are reference to 320 Ohm. The loss of bandwidth due to the ground plane is evident.

Figure 5.29: Simulated and measured far field pattern results for the planar sinuous feed at 3 GHz.

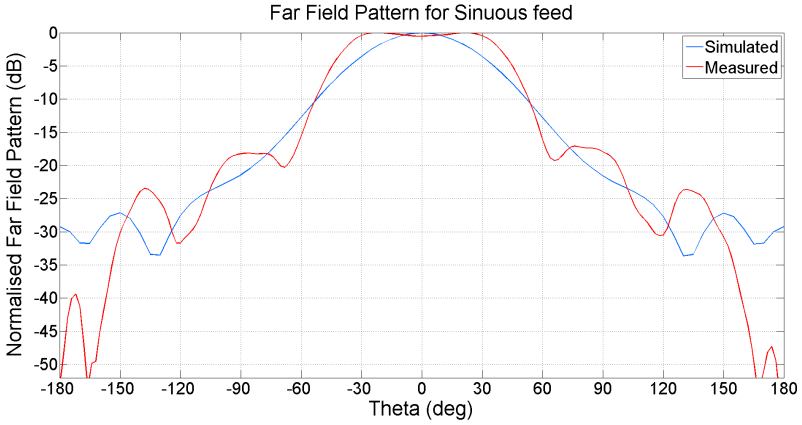

Figure 5.30: Simulated and measured far field pattern results for the planar sinuous feed at 5 GHz.

Figure 5.31: Simulated and measured far field pattern results for the planar sinuous feed at 7 GHz.

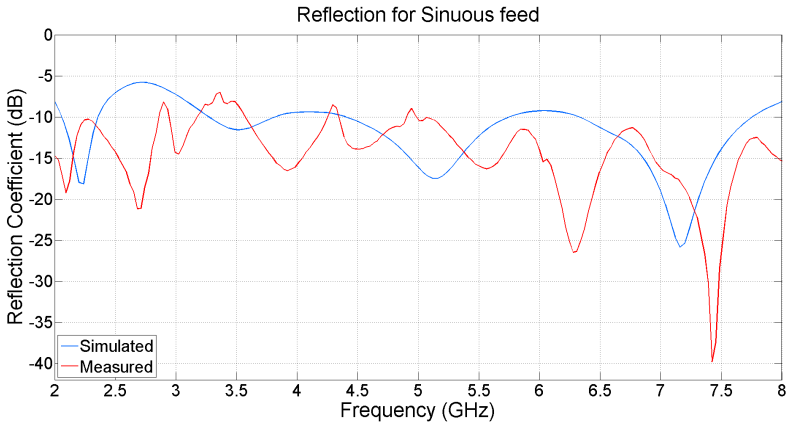

Figure 5.32: Simulated and measured reflection coefficient results for the planar sinuous feed referenced to 320 Ohm.

5.5 HERA Analysis

Having investigated and performed optimization on possible feeds for HERA, this section then appropriately looks at these feeds above a HERA faceted dish at a focal point of 4.5 m. The current backplane is included in the PAPER and bowtie models, but is not present in the sinuous model. This is due to size constraints.

The gain performance of these feeds were investigated first. As expected the gain of the PAPER dipoles and various bowtie feeds are almost identical and shown previously in Figure 4.2. The zenith gain for the remaining feeds are shown in Figure 5.33. The gain of the scaled PAPER feed shows little variation up to 120 MHz before decreasing and varying rapidly for the rest of the band. As this feed is only designed for below 120 MHz, this gain variation is not a worrying factor. Further, it is noticeable that the screen does not affect the sinuous feed in the way it does the PAPER and Bowtie feeds as there is no dip in the gain.

Figure 5.34 shows the beam patterns at $\phi = 0°$ at 150 MHz. Again, the gain properties of the various bowtie feeds are almost identical to the PAPER feed, but it is worthwhile to discuss the FoV and SLL of the scaled PAPER and sinuous feeds. Immediately noticeable is the wide beam pattern of the scaled PAPER feed forming a null at the zenith. This undesired feature is present for the entire band above 150 MHz. The maximum gain of the sinuous feed is 20.27 dB, about 4 dB weaker than the PAPER feed. Also, the FoV and SLL for the sinuous feed is computed as 10.64° and 12.89 dB, respectively. The gain near the horizon is 37.62 dB and 36.81 dB below the zenith for the scaled PAPER feed and the sinuous feed, respectively.

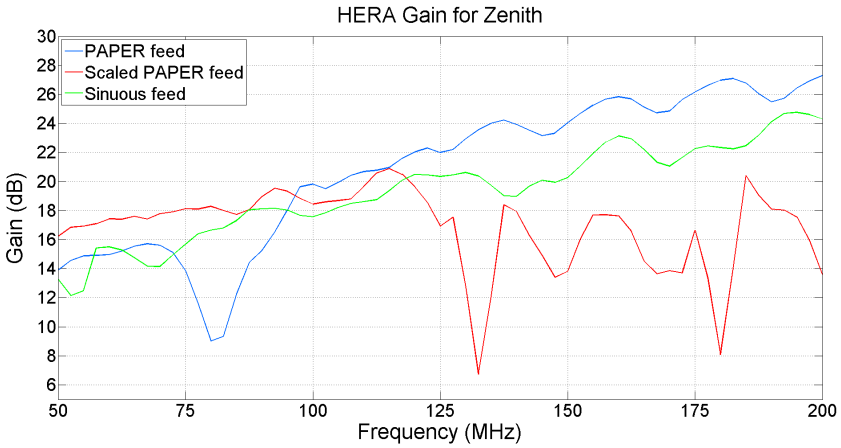

Figure 5.33: Zenith gain of the HERA dish with the PAPER feed, the bowtie feed and the sinuous feed, respectively.

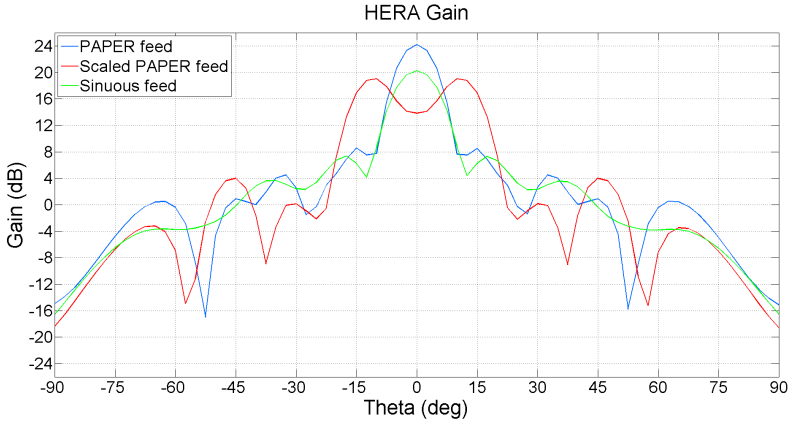

Figure 5.34: Gain for $\phi = 0°$ at 150 MHz of the HERA dish with the PAPER feed, the bowtie feed and the sinuous feed, respectively.

The reflection coefficient for HERA is shown in Figure 5.35 where each feed is referenced appropriately as mentioned in the caption. The PAPER feed delivers a operating bandwidth of approximately 125 MHz - 180 MHz. There is weak reflection for the scaled PAPER feed across the whole band which includes the operating band below 120 MHz. The sinuous feed delivers a bandwidth of approximately 80 MHz - 200 MHz which is a large improvement compared against other investigated feeds. The reflection for the various bowtie feeds are shown in Figure 5.36 and Figure 5.37. The former shows the feed not referenced to different impedances, but rather referenced to the source impedance of 50 Ohm. Although there is a limited operating bandwidth for all three cases, the effect of the modification in the bowtie and even the rounding of corners is still noticeable. Figure 5.37 shows each bowtie feed referenced appropriately as mentioned in the figure caption. This causes a null for all three cases at approximately 140 MHz with a narrow bandwidth.

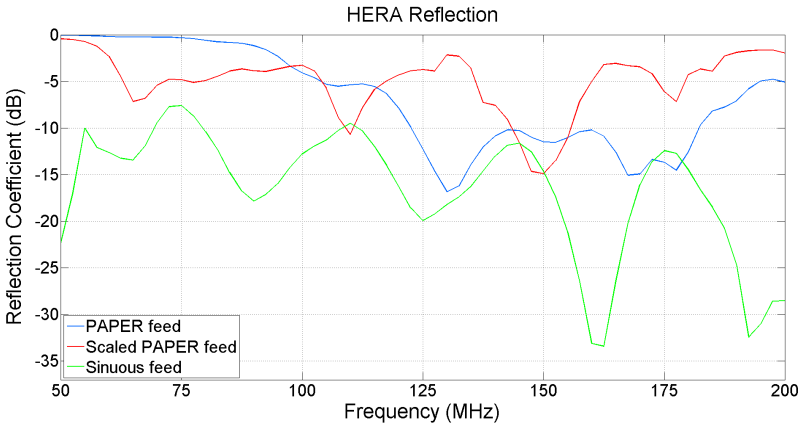

Figure 5.35: Reflection of the HERA dish with the PAPER feed referenced to 145 Ohm, the scaled PAPER feed referenced to 220 Ohm and the sinuous feed referenced to 267 Ohm.

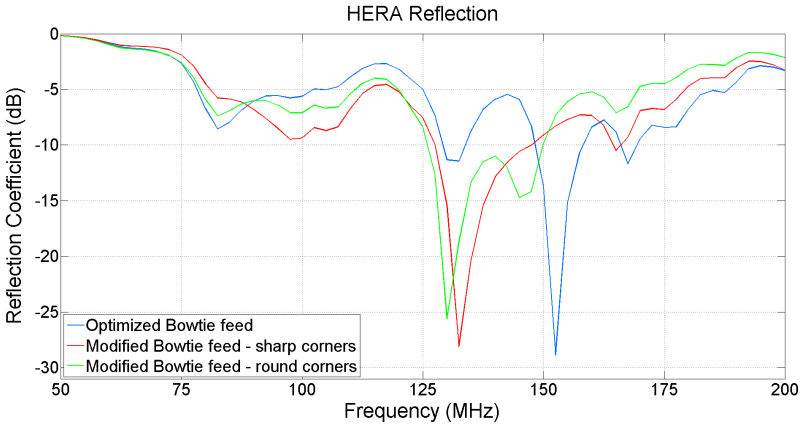

Figure 5.36: Reflection of the HERA dish with all feeds referenced to 50 Ohm.

The cross-polarization results for the sinuous feed compared to the PAPER feed for 150 MHz is shown in Figure 5.38. The bowtie feeds all have similar X-pol gain to the PAPER feed and is omitted from the plot. Also, the scaled PAPER feed has similar results to the sinuous feed and is also omitted. The $\phi = 0°$ X-pol gain of the sinuous feed is measured at -28 dB compared to the main beam with the $\phi = 45°$ case measured at -17 dB compared to the main beam.

The dish illumination is next compared. The optimized bowtie feed and the bowtie feed with round corners produce the same level of illumination as the PAPER feed in Figure 4.6. The illumination of the modified bowtie with sharp corners is shown in Figure 5.39 with better illumination compared to the PAPER feed. Also shown in Figure 5.39 is the HERA dish without a screen and the PAPER feed with a cylinder covering attached to the backplane. This cylinder covers the feed and prevents it from 'seeing' other feeds in the array. This also increases the illumination of the currents on the dish compared to

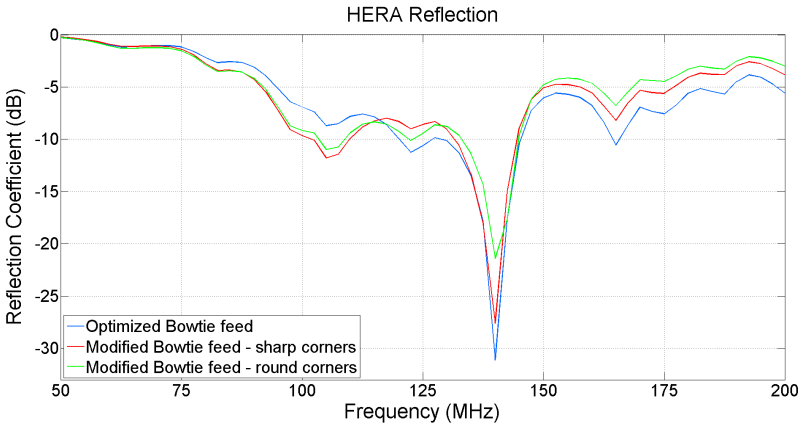

Figure 5.37: Reflection of the HERA dish with the optimized bowtie feed referenced to 150 Ohm, and the modified bowtie feed with sharp and round corners referenced to 85 Ohm and 100 Ohm, respectively.

Figure 4.6.

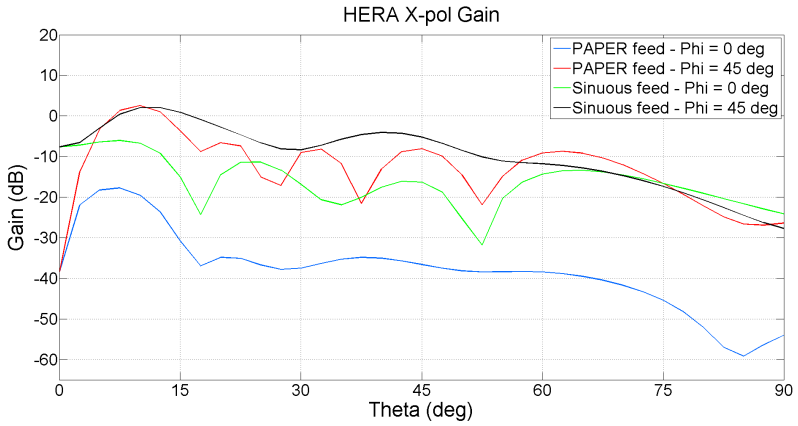

Figure 5.38: Cross-polarization for various feeds on the HERA dish.

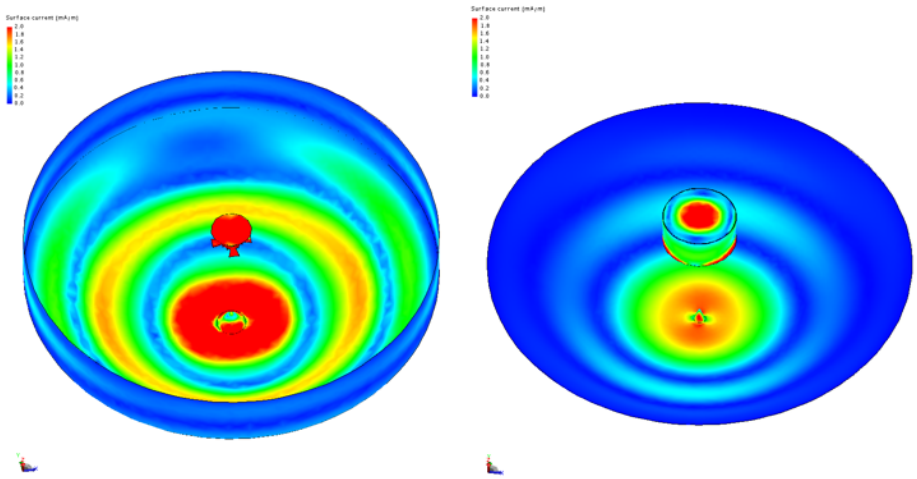

Figure 5.39: Instantaneous currents as illuminated on a HERA dish by the modified bowtie feed with sharp corners (left) at 150 MHz and the PAPER feed with cylinder as covering (right) at a phase of 90°.

5.5.1 Time-domain Analysis

The reflection specification of −60 dB by 60 ns was already investigated for the HERA dish in Chapter 4.4 where it was shown that the PAPER feed does not satisfy this specification. It can be stated that these reflections are dependent on the reflectometry and the S11 parameter of the antenna. Of course, the dish and focal distance for all feeds investigated in this chapter are similar which implies that a difference in results is due to the difference in the reflection coefficient of each feed.

The response of the antenna is initially obtained in the form of the S11 parameter as a function of frequency. The response R in the time-domain is obtained by converting frequency domain POSTFEKO results using FFTs. Finally, deconvolution of the input signal and the response signal is applied to obtain the output signal. To illustrate the effect of a matched feed on the reflection specification, the ideal case where only the secondary reflections returns into the feed is shown in the following results. Figure 5.40 shows the FEKO results for the PAPER feed when it is mathematically terminated in its characteristic impedance. The reflected signal in dB is shown in Figure 5.41 where it can be seen that the reflection specification is narrowly met. This is a significant improvement over the unmatched system investigated in Chapter 4.4.

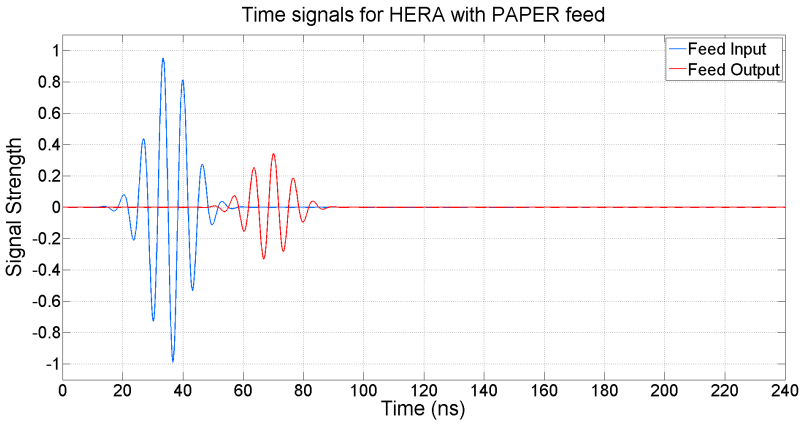

Figure 5.40: Time-domain input and output signals for the HERA dish when the PAPER feed is terminated in its characteristic impedance, hence, only showing the secondary reflection on the output signal.

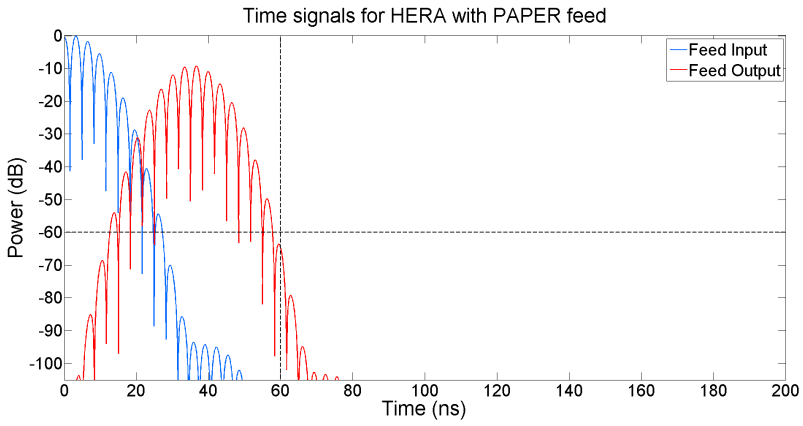

Figure 5.41: Time-domain input and output power signals for the HERA dish when the PAPER feed is terminated in its characteristic impedance.

5.6 Conclusion

This chapter investigated and electromagnetically analyzed possible feeds for the HERA parabolic dish by comparing them to the current PAPER feed. The PAPER feed is inherently a narrowband antenna which allowed for much room for improvement. Even though the different versions of the bowtie feed show improved results, the sinuous antenna met this criteria covering the whole $50-200$ MHz operating band. The scaled PAPER feed is a possibility for the lower band of $60-120$ MHz, but does not show promising results on the HERA dish. Also, the advantage of a well matched system was shown by minimizing the effect of the overall reflections on the dish.

Chapter 6

Conclusions and Recommendations

6.1 Conclusions

This chapter concludes this thesis by appropriately making informed recommendations on the specification for the HERA dish and feed based on results shown in preceding chapters. This section is succeeded by a description of contributions made specifically to the HERA collaboration followed by recommendations for future work.

Table 6.1 is a duplicate of Table 4.1 in Chapter 4.2. However, the former is the HERA performance based on simulation results and not pre-specified values. The frequency range, dish diameter, focal length and geometrical optics is fixed by either science or cost efficiency. Furthermore, unlike the reflections specification, the beam near horizon and FoV approximately meet their original estimates. The SLL is measured at 15.63 dB for 150 MHz. For a parabolic reflector at higher frequencies, with a good feed taper, the expected SLL would be within the range of 30 dB. However, the low frequency HERA band has the ability to alter this specification considerably. The cross-polarization is measured at -21 dB compared to the main beam. The HERA element has a slow gain variation across frequency with an average of 3 dB/25 MHz. This is a significant result as it has direct influence on the instrument's ability to isolate foregrounds. However, overall the HERA dish is not a good reflector as measured by most performance parameters.

With the PAPER antenna element indeed performing well enough to produce science at such low frequencies, it was found that to produce a better alternative feed for EoR science is not an easy task. This is emphasized in the effort to produce a feed for the lower extended band in the form of a scaled PAPER feed. Even though the dipoles introduce smooth gain across frequency, the feed is poorly matched. One trade-off is between element size and bandwidth. As was demonstrated by the sinuous and bowtie feeds, the

larger the element (or wider the angle), the larger the bandwidth. The geometrical size constraints that accompanies the wide bandwidth is something to be considered as this also introduces aperture blockage.

Parameter	**Original Estimate**	**Performance**
Frequency range	108−200 MHz (performance), 60 − 200 MHz (extended)	-
Diameter	14 m	-
Focal length	4.5 m ($f/d = 0.32$)	-
Geometrical optics	prime focus, faceted paraboloid	-
FoV @ 150 MHz	9°	8.9°
SLL @ 150 MHz	TBD	15.63 dB
Maximum Gain @ 150 MHz	TBD	24.19
Beam near horizon @ 150 MHz	$<$ −40 dB compared to zenith	−39.31 dB compared to zenith
Cross-polarization	TBD	−21 dB compared to main beam
Gain variation across frequency	TBD	Average of 3 dB/25 MHz
Reflections	−60 dB at 60 ns	−35 dB at 60 ns
Surface accuracy	75 mm	12 mm
Characteristic Impedance	50 Ohm (LNA)	-

Table 6.1: HERA specifications compared to performance based on simulation results.

6.2 Contributions

The HERA analog collaborative group played a fundamental part in the forming of this thesis. The author was part of the main analog bi-weekly discussions on the dish and feeds and eventually played a part in the design of and discussions around the scaled PAPER feed and sinuous feed.

The following contributions were made to the HERA collaborative network. Firstly, the differences between a perfect paraboloid and a faceted paraboloid have been established. FEKO results were also provided and compared with CST results to investigate their validity. The author worked with NRAO and MIT on the scaled PAPER feed and sinuous feed. This includes the design of the sinuous feed and FEKO modelling and analysis. High resolution beam-mapping FEKO data of the HERA dish have been provided to collaborators to inspect its influence on EoR data.

6.3 Recommendations and Future Work

HERA is an active experiment with more phases still to come, which means future work can be applied in terms of designing and analysing improved dishes and feeds. Further investigation into low frequency feeds for radio astronomy is thus recommended.

Also, investigation into solutions for problems caused by reflections would be worthwhile. One solution could be offered by different absorbing materials which are placed in the centre of the dish to mitigate vertical reflections. Also, to improve the performance of the reflector, investigation of an off-set dish is possible. This would not be practical for the complete array, but could be considered for a small part thereof. The major advantage of this design is the prevention of secondary reflections. However, the implications of the reflections on the EoR signal is further investigated in [24] where it is shown that isolation of EoR signals for a certain redshift value would still be detectable with a -40 dB reflection signal.

Appendices

Appendix A

Study of Low Frequency Arrays

A.1 Introduction

The low frequency arrays LOFAR and MWA discussed in this Appendix were designed and built as an innovative effort to establish a breakthrough in sensitivity for astronomical observations at radio-frequencies below 300 MHz.

A.2 LOFAR

A.2.1 Background

The Low Frequency Array (LOFAR) is a radio telescope designed by ASTRON and located across Europe. Elements in the core area of these stations are nearly adjacent with outliers with distances of up to 80 km. LOFAR is optimized for the unexplored low frequency range from $30-240$ MHz. With its dense core array and long baselines, LOFAR is intended to reach unmatched sensitivity and spatial resolution in the low frequency radio range [29].

A.2.2 Antenna Analysis

The LOFAR band is covered by two antenna types namely a Low Band Antenna (LBA) and a High Band Antenna (HBA) for the $30-80$ MHz and $120-240$ MHz range, respectively, with both antennas dual polarized. Both antennas are shown in Figure A.1.

The LBA's are droop dipoles above a conducting ground plane with the wires at an angle of 45° to the ground (i.e. inverted V-shaped dipoles). The dipoles are positioned at 1.7 m, a compromise between high and low frequency performance, above a 3×3 m square ground plane. The HBA's are vertical bowties of 45 cm height grouped into sub-arrays or tiles of 4×4 elements [29].

Usually wideband antennas covering frequencies as low as 30 MHz exceeds the maximum height above the ground plane of 2 m. However, in this case

Figure A.1: Low-band (left) and high-band (right) antenna elements for LOFAR (Source: David Davidson).

the LBA is a receive only antenna which allows the use of an active balun. Figure A.2 shows the zenith gain across frequency of a single LBA element for three different heights. These heights are measured between the ground and the feed-point of the antenna. In a similar way as the sinuous feed, the LBA element also experiences a null in the gain when the antenna is lifted above the minimum height. At 1.7 m the antenna element has a directivity that increases from 2 dB to 7 dB up to 65 MHz and decreases to 5.7 dB down to 80 MHz.

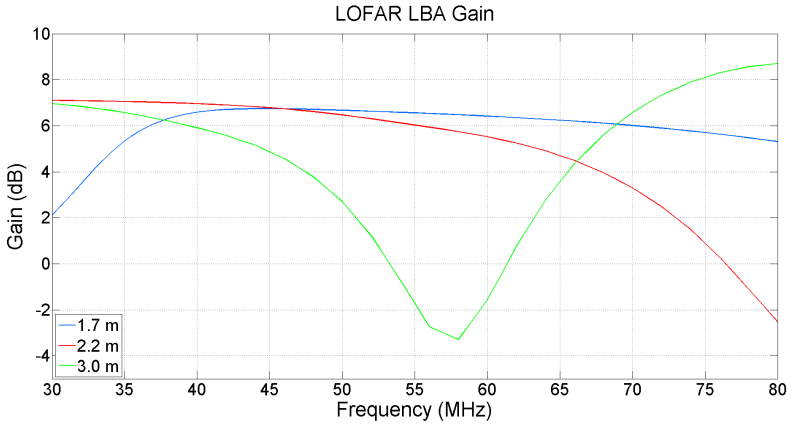

Figure A.2: Zenith Gain for the LOFAR low band antenna element for different heights above the ground plane.

The antenna performance is limited below 30 MHz because of the dipole's radiation characteristics [29]. The radiation pattern of the dipoles are not significantly altered when bending the dipoles, but there occurs broadening of the main lobe causing a small decrease in the main lobe gain. The radiation pattern is required to be broad to maximise sensitivity at low elevations. The LBA element produces a FoV of approximately 82° at 50 MHz.

Figure A.3 shows the real and imaginary input impedance for the LBA element with a height of 1.7 m. There is a resonance at approximately 52 MHz with real impedance values reaching into the triple digits Ohms across the band. The effect of this can be seen in the reflection results in Figure A.4 where all cases are referenced to 152 Ohm. The narrowband effect of the dipole can be seen. It is worth noting that neither a balun nor a matching network is included in these results.

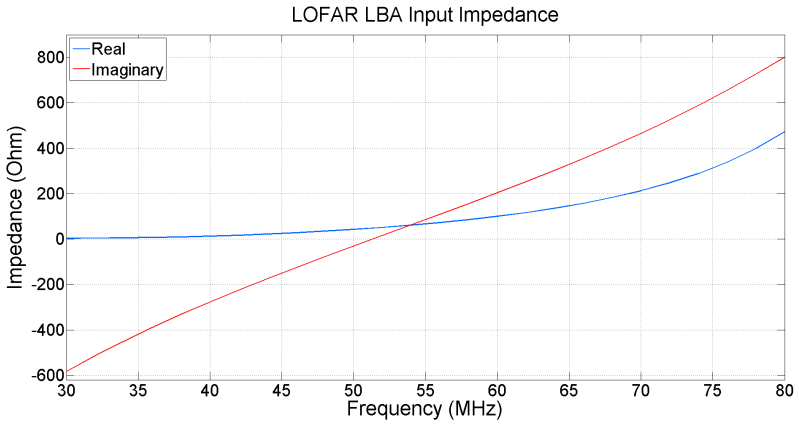

Figure A.3: Input impedance for the LOFAR low band antenna element with a height of 1.7 m above the ground plane.

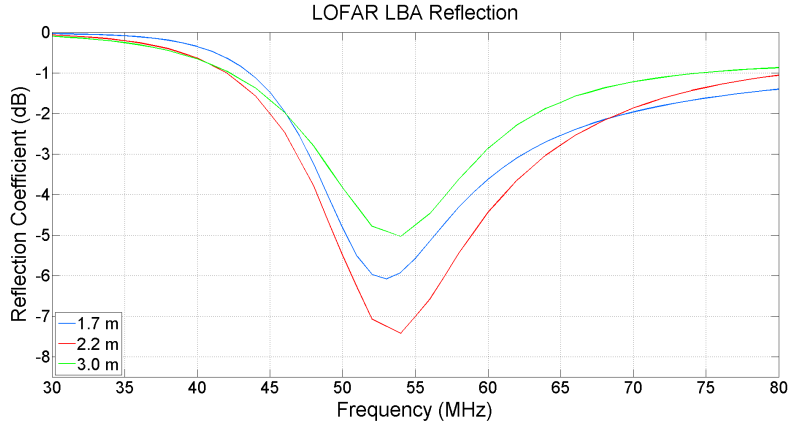

Figure A.4: Reflection referenced to 152 Ohm for the LOFAR low band antenna element for different heights above the ground plane.

Advantages of using dipoles for radio astronomy application include the fact that they are cost-effective and simple to manufacture or install. Also, in the case of LOFAR, the omnidirectional radiation pattern above ground of the dipoles allows for instantaneous imaging of very wide fields. Also, the "droopy" or V-shaped dipoles cause the physical shape of the antenna to be

decreased and can be advantageous specifically in arrays where the elements are in close proximity to each other.

The LOFAR HBA elements were not modelled in FEKO, but the performance of a MWA bowtie antenna is investigated in the next section. Bowtie antennas are in essence the planar cross-sections of biconical antennas [28]. Their radiation pattern are superior to those of a simple and "droopy" dipole. Biconical antennas has poor efficiency at low frequencies which results in low field strengths relative to the input power [28].

A.3 MWA

A.3.1 Background

The Murchison Widefield Array (MWA) is an array telescope designed to operate in the $80 - 300$ MHz range where brightness temperature fluctuations during the EoR is one of the science goals. The array design features 8192 elements, arranged into 512 tiles consisting of 16 elements each. The tiles are distributed in a core covering an aperture 1.5 km in diameter, with a small number of outliers extending to it to 3 km. The array is located in the Murchison region of Western Australia which is known to have an extremely low population density and is a excellent radio-quiet environment [34].

A.3.2 Antenna Analysis

The MWA antenna element is a pair of vertical bowties which are orthogonal to each other and span over 74 cm. 16 elements are placed in a single tile and is shown in Figure A.5. This design secures for a wide instantaneous FoV causing minimal gain at the horizon [35]. Thus, the MWA is able to collect useful imaging information for a larger part of the sky for a single observation than an array of equal collecting area consisting of larger elements [34].

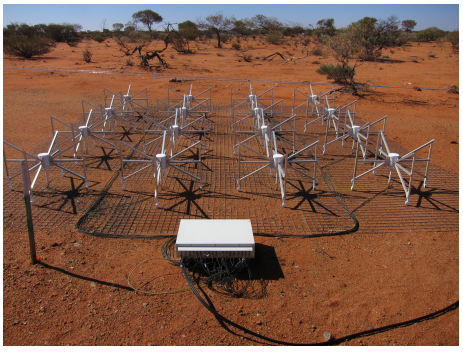

Figure A.5: 16 MWA elements on a single tile (Source: David Davidson).

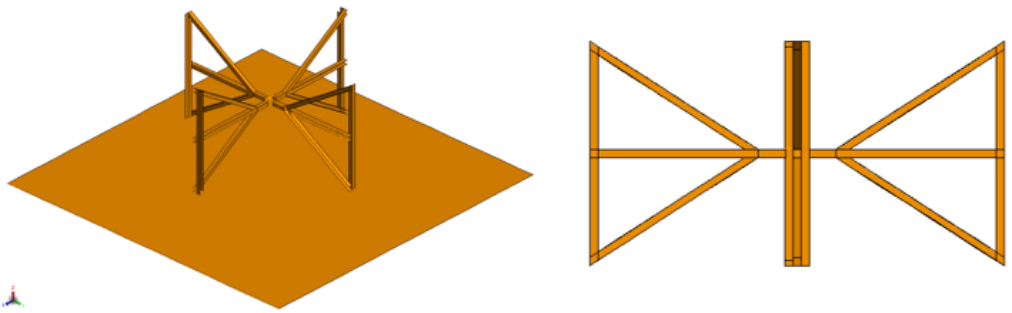

Figure A.6: A FEKO model of the MWA antenna element with ground plane (left) and bowtie sideview (right).

The FEKO model for the MWA bowtie with ground plane is shown in Figure A.6. The gain is shown in Figure A.7 where there is almost no variation in the mid to high band which is desirable. The FEKO model also delivers a HPBW of approximately 90° at 150 MHz

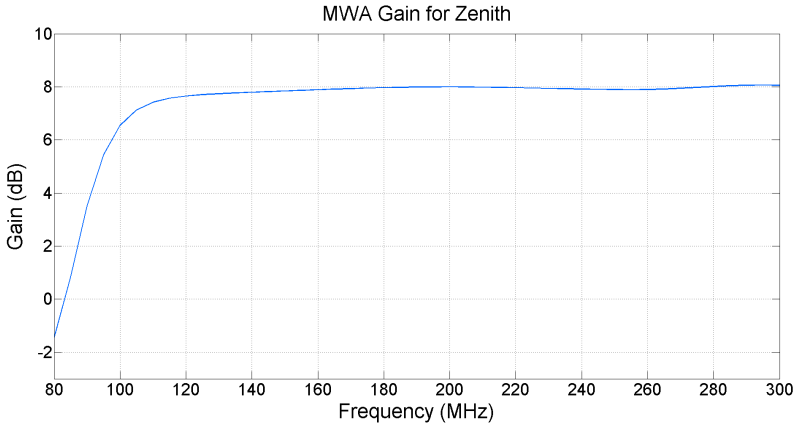

Figure A.7: Gain for zenith of a single MWA element.

The input impedance is shown in Figure A.8 and shows a dual-resonance across the band at approximately 115 MHz and 250 MHz. Although there exists a deep null in the reflection at the first resonance when referenced to 50 Ohm, the rest of the band is not well matched. The reflection seen in Figure A.9 is matched to 200 Ohm and shows −3 dB reflection for the mid and upper band. It is worthwhile to note that the MWA uses active elements where matching is not particularly crucial. As is the case for the LOFAR FEKO model, a balun or matching network is not included in the design. It was found that removing the spar in the middle of the bowties deteriorates the reflection even further.

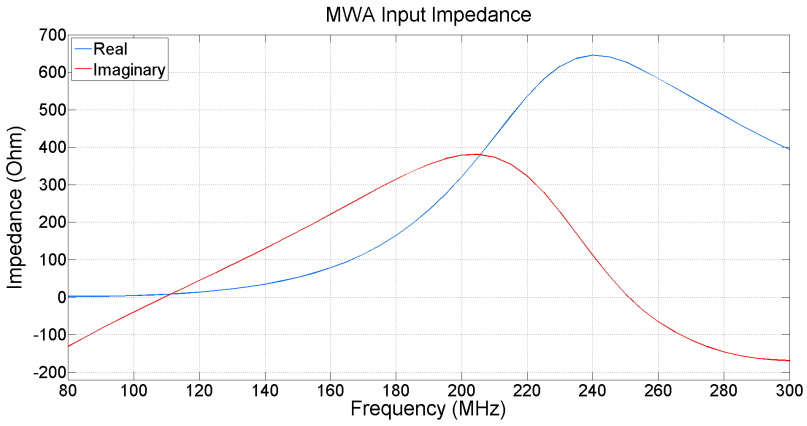

Figure A.8: Input impedance of a single MWA element.

Figure A.9: Reflection referenced to 200 Ohm of a single MWA element.

Due to the element's wide FoV there exists mutual coupling between the closed-packed elements which makes it increasing difficulty to detect faint sources in the midst of bright sources concealing them. The mutual coupling between two adjacent elements as well as two elements on the edge of the tile is shown in Figure A.10. The S31 parameter represents coupling from two co-polarized feeds on adjacent elements. The coupling is between -10 dB and -40 dB which is a worrisome result. The X-polarized result or S41 parameter is down by approximately 15 dB across the band which is expected. However, it is still not ignorable at the lower frequencies of the band where the coupling reaches -22 dB. The two parameters representing the coupling of two elements on opposite edges of the tile shows expected improved results. The mutual coupling ranges from approximately -40 dB to -80 dB.

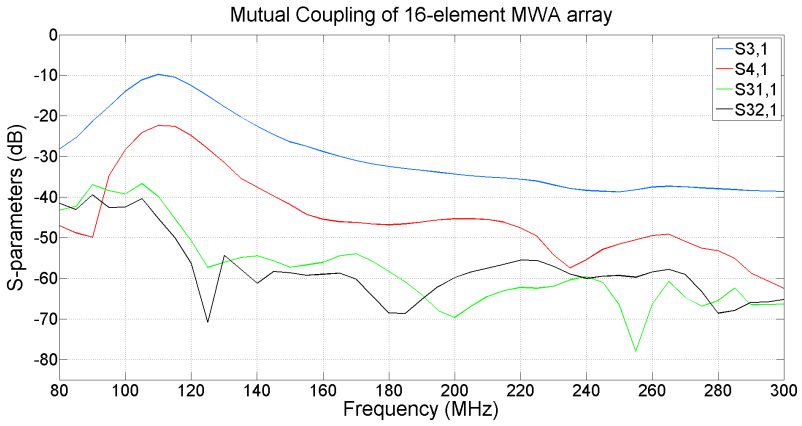

Figure A.10: Selected S-parameters of a 16-element MWA array representing mutual coupling between adjacent elements and elements on the edge of the tile.

A.4 Conclusion

EM modelling and analysis of the LOFAR and MWA arrays give insight into the workings of low frequency arrays used for radio astronomy. This was done as a first step before embarking on deeper investigation of HERA.

Appendix B

Mathematical Theorems & Formulas

B.1 Green's Theorem

To derive Green's theorem it is needed to make use of the divergence theorem which states that for any arbitrary vector **A** "the closed surface integral of the normal component of vector **A** over a surface S is equal to the volume integral of the divergence of **A** over the volume V enclosed by S" [18]. This in mathematical form is stated as

$$\int_v \nabla \cdot \mathbf{A}\, dv = \oint_s \mathbf{A} \cdot d\mathbf{s}\,. \tag{B.1.1}$$

Also, defining $\mathbf{A} = \phi\nabla\psi$, where ϕ is a scalar field and $\nabla\psi$ a vector field, the divergence of **A** would be

$$\nabla \cdot \mathbf{A} = \nabla\phi \cdot \nabla\psi + \phi\nabla^2\psi\,. \tag{B.1.2}$$

Substituting Equation B.1.2 into Equation B.1.1

$$\int_v \phi\nabla^2\psi\, dv + \int_v \nabla\phi \cdot \nabla\psi\, dv = \oint_s \phi\nabla\psi \cdot d\mathbf{s}\,. \tag{B.1.3}$$

This is known as Green's first identity in scalar form. By interchanging ϕ and ψ and subtracting Equation B.1.3 from the same but interchanged equation, Green's second identity or Green's theorem in scalar form is formulated as

$$\int_v [\phi\nabla^2\psi - \psi\nabla^2\phi]\, dv = \oint_s [\phi\nabla\psi - \psi\nabla\phi] \cdot d\mathbf{s}\,. \tag{B.1.4}$$

Also, Green's theorem in scalar-vector form is

$$\int_V [b(\nabla \times \nabla \times \mathbf{a}) + \mathbf{a}\nabla^2 b + (\nabla \cdot \mathbf{a})\nabla b]\, dV$$
$$= \oint_S [(\hat{n} \cdot \mathbf{a})\nabla b + (\hat{n} \times \mathbf{a}) \times \nabla b + (\hat{n} \times \nabla \times \mathbf{a})b]\, dS\,. \quad \text{(B.1.5)}$$

B.2 Differential S-parameters

The standard S-parameters for a single-ended device with four ports is

$$S_{std} = \begin{bmatrix} S_{11} & S_{12} & S_{13} & S_{14} \\ S_{21} & S_{22} & S_{23} & S_{24} \\ S_{31} & S_{32} & S_{33} & S_{34} \\ S_{41} & S_{42} & S_{43} & S_{44} \end{bmatrix}\,. \quad \text{(B.2.1)}$$

However, if the same device is seen as a 2-port differential device, the mixed-mode S-parameter matrix is

$$S_{mm} = \begin{bmatrix} S_{d1d1} & S_{d1d2} & S_{d1c1} & S_{d1c2} \\ S_{d2d1} & S_{d2d2} & S_{d2c1} & S_{d2c2} \\ S_{c1d1} & S_{c1d2} & S_{c1c1} & S_{c1c2} \\ S_{c2d1} & S_{c2d2} & S_{c2c1} & S_{c2c2} \end{bmatrix}\,, \quad \text{(B.2.2)}$$

where differential port 1 is formed by port 1 and port 2 and differential port 2 formed by port 3 and port 4. To transform between the matrices in Equation B.2.1 and Equation B.2.2 a transformation matrix M, defined as

$$M = \frac{1}{\sqrt{2}} \begin{bmatrix} 1 & -1 & 0 & 0 \\ 0 & 0 & 1 & -1 \\ 1 & 1 & 0 & 0 \\ 0 & 0 & 1 & 1 \end{bmatrix}\,, \quad \text{(B.2.3)}$$

can be used to give the relationship of

$$S_{mm} = M S_{std} M^{-1}\,. \quad \text{(B.2.4)}$$

Bibliography

[1] F. Ghigo. (2008) Karl Jansky and the discovery of cosmic radio waves. [Online]. Available: http://www.nrao.edu/whatisra/hist_jansky.shtml

[2] ——. (2004) Grote Reber and his radio telescope. [Online]. Available: http://www.nrao.edu/whatisra/hist_reber.shtml

[3] SKA-SA. (2014) Everything you wanted to know about the SKA. [Online]. Available: http://www.ska.ac.za/qa/index.php

[4] M. Richmond. (2014) The interstellar medium: Gas. [Online]. Available: http://spiff.rit.edu/classes/phys230/lectures/ism_gas/ism_gas.html

[5] SUT. (2014) Spin-flip transition. [Online]. Available: http://astronomy.swin.edu.au/cosmos/S/Spin-flip+Transition

[6] J. Hawley. (1999) Redshift. [Online]. Available: http://www.astro.virginia.edu/~jh8h/glossary/redshift.htm

[7] C. A. Balanis, *Antenna theory: analysis and design*, 3rd ed. John Wiley & Sons, Inc., 2005.

[8] S. Silver, *Microwave Antenna Theory and Design*. McGraw-Hill, 1949, vol. 12.

[9] J. Ruze, *Physical Limitations of Antennas*. MIT Res. Lab. Electron. Tech. Rept, 1952.

[10] R. DuHamel and D. Isbell, "Broadband logarithmically periodic antenna structures," *IRE National Convention Record*, no. 1, pp. 119–128, 1957.

[11] R. DuHamel, "Dual polarized sinuous antennas," Patent (U.S.) 4 658 262, April, 1987.

[12] G. Deschamps, "Impedance properties of complementary planar structures," *IRE Trans Antennas and Propagation*, vol. AP-7, no. 1, pp. S371–378, Dec 1959.

[13] A. Thompson, J. Moran, and G. Swenson, *Interferometry and Synthesis in Radio Astronomy*, 2nd ed. Wiley-VCH Verlag, 2004.

[14] S. Muchovej, "Interferometry," SKA Radio Astronomy Workshop, 2014.

[15] A. Parsons and D. Backer, "Calibration of low-frequency, wide-field radio interferometers using delay/delay-rate filtering," *The Astronomical Journal*, vol. 138, pp. 219–226, July 2009.

[16] A. Parsons, J. Pober, J. Aguirre, L. Carilli, D. Jacobs, and D. Moore, "A per-baseline, delay-spectrum technique for accessing the 21 cm cosmic reionization signature," *The Astronomical Journal*, vol. 756, pp. 165–180, September 2012.

[17] J.-M. Jin, *Theory and Computation of Electromagnetic Fields*. John Wiley & Sons, Inc., 2010.

[18] C. A. Balanis, *Advanced Engineering Electromagnetics*, 2nd ed. John Wiley & Sons, Inc., 2012.

[19] S. Rao, D. Wilton, and R. Mittra, "Electromagnetic scattering by surfaces of arbitrary shape," *IEEE Trans. Antennas Propagat.*, vol. 30, no. 3, pp. 409–418, May 1982.

[20] D. B. Davidson, *Computational electromagnetics for RF and microwave engineering*, 2nd ed. Cambridge University Press, 2011.

[21] EMSS, *FEKO Suite 6.1 User's Manual*, 2011.

[22] T. Weiland, "A discretization method for the solution of Maxwell's equations for six-component fields," *Electron. Commun. (AEU)*, vol. 31, no. 3, pp. 116–120, 1977.

[23] A. Parsons and D. deBoer, "Configuration of the HERA element (Memo)," May 2015.

[24] A. Ewall-Wice, N. Abraham, P. Nipanjana, N. Thyagarajan, R. Bradley, J. Hewitt, A. Zaki, J. Bowman, C. Cheng, D. deBoer, A. Parsons, and M. Venter, "The Hydrogen Epoch of Reionization Array dish: characterization with electromagnetic simulations (Draft)," November 2015.

[25] A. Ewall-Wice, J. Hewitt, R. Bradley, and M. Venter, "Simulations of the delay response of the HERA dish implications for EoR power spectrum measurements (Memo)," September 2015.

[26] A. Parsons, D. Backer, and G. Foster, "The Precision Array for Probing the Epoch of Re-ionization: Eight station results," *The Astronomical Journal*, 2010.

[27] A. Poggio and P. Mayes, "Pattern bandwidth optimization of the sleeve monopole antenna," *Antennas and Propagation, IEEE Transactions on*, vol. 14, no. 5, pp. 643–645, Sep 1966.

[28] C. A. Balanis, *Modern Antenna Handbook*, 3rd ed. John Wiley & Sons, Inc., 2008.

[29] R. Vermeulen and M. Van Haarlem, "The international LOFAR telescope (ILT)," in *General Assembly and Scientific Symposium, 2011 XXXth URSI*, Aug 2011.

[30] R. Pierce, S. Aroor, A. Blanchard, and R. Henderson, "Broadband millimeter wave modified aperture bowtie antenna-in-package," *Texas Symposium on Wireless and Microwave Circuits and Systems (WMCS)*, pp. 1–4, April 2013.

[31] N. Mutonkole, "Study of a wideband sinuous feed for reflector antenna applications," Master's thesis, Stellenbosch University, December 2013.

[32] D. Prinsloo, P. Meyer, R. Maaskant, and M. Ivashina, "Design of an active dual-mode antenna with near hemispherical field of view coverage," *International Conference on Electromagnetics in Advanced Applications (ICEAA)*, pp. 1064–1067, September 2013.

[33] W. Fan, A. Lu, L. Wai, and B. Lok, "Mixed-mode S-parameter characterization of differential structures," *Electronics Packaging Technology, 2003 5th Conference*, pp. 533–537, 2003.

[34] C. Lonsdale, R. Cappallo, M. Morales, F. Briggs, L. Benkevitch, J. Bowman, J. Bunton, S. Burns, B. Corey, L. deSouza, S. Doeleman, M. Derome, A. Deshpande, M. Gopala, L. Greenhill, D. Herne, J. Hewitt, P. A. Kamini, J. Kasper, B. Kincaid, J. Kocz, E. Kowald, E. Kratzenberg, D. Kumar, M. Lynch, S. Madhavi, M. Matejek, D. Mitchell, E. Morgan, D. Oberoi, S. Ord, J. Pathikulangara, T. Prabu, A. Rogers, A. Roshi, J. Salah, R. Sault, N. Shankar, K. S. Srivani, J. Stevens, S. Tingay, A. Vaccarella, M. Waterson, R. Wayth, R. Webster, A. Whitney, A. Williams, and C. Williams, "The Murchison Widefield Array: Design overview," *Proceedings of the IEEE*, vol. 97, no. 8, pp. 1497–1506, Aug 2009.

[35] MWA. (2014) Murchison Widefield Array - antenna/beamformer. [Online]. Available: http://www.mwatelescope.org/telescope/antenna-beamformer